VANADIUM OXIDE (VO_x) THIN FILMS ELABORATED BY SOL-GEL METHOD FOR MICROBOLOMETER APPLICATIONS

A THESIS SUBMITTED TO
THE GRADUATE SCHOOL OF NATURAL AND APPLIED SCIENCES
OF
MIDDLE EAST TECHNICAL UNIVERSITY

BY

KADİR KARSLI

IN PARTIAL FULFILLMENT OF THE REQUIREMENTS
FOR
THE DEGREE OF MASTER OF SCIENCE
IN
MICRO AND NANOTECHNOLOGY

JANUARY 2012

Approval of the thesis:

VANADIUM OXIDE (VO_x) THIN FILMS ELABORATED BY SOL-GEL METHOD FOR MICROBOLOMETER APPLICATIONS

submitted by **KADİR KARSLI** in partial fulfillment of the requirements for the degree of **Master of Science in Micro and Nanotechnology Department, Middle East Technical University** by,

Prof. Dr. Canan Özgen _____
Dean, Graduate School of **Natural and Applied Sciences**

Prof. Dr. Mürvet Volkan _____
Head of Department, **Micro and Nanotecnology**

Prof. Dr. Tayfun Akın _____
Supervisor, **Electrical and Electronics Engineering Dept., METU**

Assoc. Prof. Dr. Caner Durucan _____
Co-Supervisor, **Metallurgical and Materials Eng. Dept., METU**

Examining Committee Members:
Prof. Dr. Raşit Turan _____
Physics Dept., METU

Prof. Dr. Tayfun Akın _____
Electrical and Electronics Engineering Dept., METU

Assoc. Prof. Dr. Caner Durucan _____
Metallurgical and Materials Engineering Dept., METU

Assoc. Prof. Dr. Haluk Külah _____
Electrical and Electronics Engineering Dept., METU

Dr. M. Yusuf Tanrıkulu _____
Research Fellow, METU-MEMS Center

Date: 24 January 2012

I hereby declare that all information in this document has been obtained and presented accordance with the academic rules and ethical conduct. I also declare that, as required by these rules and conduct, I have fully cited and referenced all material and results that are not original to this work.

Name, Last name : Kadir KARSLI

Signature :

ABSTRACT

VANADIUM OXIDE (VO_x) THIN FILMS ELABORATED BY SOL-GEL METHOD FOR MICROBOLOMETER APPLICATIONS

Karslı, Kadir

M.Sc., Department of Micro and Nanotechnology

Supervisor: Prof. Dr. Tayfun Akın

Co-Supervisor: Assoc. Prof. Dr. Caner Durucan

January 2012, 104 pages

Infrared detector technologies have been developing each day. Thermal detectors take great attention in commercial applications due to their low power consumption and low costs. The active material selection and the deposition of the material are highly important performance effective factors for microbolometer detector applications. In that sense, developing vanadium oxide (VO_x) microbolometer active material by sol-gel method might be feasible approach to achieve good performance microbolometer detectors.

In this study, vanadium oxide thin films are prepared by sol-gel method is deposited on silicon or silicon nitride wafers as active material by spin coating. The films are annealed under different hydrogen concentration of H_2/N_2 environments at 410 °C for various hours to obtain desired oxygen phases of vanadium oxide thin films. After appropriate annealing step, V_2O_5 structured thin films are reduced to mixture of lower oxygen states of vanadium oxide thin films which contains V_2O_5, V_6O_{13}, and VO_2. Finally, the performance parameters such as sheet resistance, TCR, and noise are measured to verify the quality of the developed vanadium oxide active layers for their use in microbolometers. The sheet resistances are in the range of 100 kΩ/sqr – 200 kΩ/sqr. The resistances are reasonable values around 100 kΩ under 20 μA bias, and the TCR values of the samples measured around 2%/°C at

room temperature (25 °C). The measured noise of the films is higher than expected values, and the corner frequencies are more than 100 kHz. The results of the measurements show that it is possible to use sol-gel deposited vanadium oxide as a microbolometer active material after improving the noise properties of the material.

Keywords: Thermal detector, microbolometer, active material, vanadium oxide, sheet resistance, TCR, noise.

ÖZ

MİKROBOLOMETRE UYGULAMALARI İÇİN SOL-JEL YÖNTEMİYLE HAZIRLANAN VANADYUM OKSİT (VO_x) İNCE FİLMLER

Karslı, Kadir

Y. Lisans, Mikro ve Nanoteknoloji

Tez Yöneticisi: Prof. Dr. Tayfun Akın

Ortak Tez Yöneticisi: Doç. Dr. Caner Durucan

Ocak 2012, 104 sayfa

Kızılötesi dedektör teknolojiler her geçen gün gelişmeye devam ediyor. Düşük enerji tüketimi ve düşük fiyatları dolayısıyla ısıl dedektörler ticari uygulamalarda büyük ilgi görmektedirler. Mikrobolometre için aktif malzeme seçimi ve bu malzemenin ince film olarak uygulanması dedektör uygulamalarında performansa önemli derecede etki etmektedir. Sol-jel yöntemiyle üretilen vanadyum oksit mikrobolometre aktif malzemeler yüksek performans mikrobolometre dedektör üretimi için iyi bir seçenek olarak gözükmektedir.

Bu tez çalışması kapsamında sol-jel yöntemi ile hazırlanan vanadyum oksit solüsyon döndürerek (spin) kaplama yöntemiyle silikon ve silikon-nitrat üzerine kaplanmıştır. Geliştirilen örnekler, farklı hidrojen oranına sahip H_2/N_2 ortamlarında 410 °C'de çeşitli sürelerde fırınlanarak istenilen oksijen seviyelerinde vanadyum oksit ince filmler elde edilmesi hedeflenmiştir. Uygun fırınlama koşullarında fırınlanan V_2O_5 yapısına sahip ince filmler daha düşük oksijen seviyelerine indirgenerek V_2O_5, V_6O_{13}, ve VO_2 seviyelerini bir arada bulunduran vanadyum oksit ince filmler elde edilmiştir. Bu filmlerin yüzey dirençleri, TCR ve gürültü seviyeleri ölçülerek mikrobolometre uygulamalarında kullanım durumları değerlendirilmiştir. Elde edilen filmlerin yüzey dirençleri 100 kΩ/sqr – 200 kΩ/sqr aralığında ölçülmüştür. İnce filmlerin, direnç değerleri makul seviyelerde olup 20 μA ön akım altında 100 kΩ

civarında, TCR değerleri ise yaklaşık 2%/ºC ölçülmüştür. Ancak gürültü seviyeleri beklenin üstünde çıkmıştır. Elde edilen sonuçlar gürültü özellikleri düzeltilmesi halinde sol-jel yöntemi ile kaplanan vanadyum oksidin mikrobolometre uygulamalarında kullanabileceğini göstermektedir.

Anahtar kelimeler: Isıl dedektör, mikrobolometre, aktif malzeme, vanadyum oksit, yüzey direnci, TCR, gürültü

To My Beloved Wife

ACKNOWLEDGEMENTS

First, I would like to express my gratitude to my supervisor Prof. Dr. Tayfun AKIN for his supervision, guidance, support, and encouragement during the study. Without his knowledge and support I would not complete this study. I would also like to thank my co-supervisor Assoc. Prof. Dr. Caner Durucan for his ideas, comments, and suggestions.

I am grateful to all of the thesis jury committee members, Prof. Dr. Raşit Turan, Prof. Dr. Tayfun Akın, Assoc. Prof. Dr. Caner Durucan, Assoc. Prof. Dr. Haluk Külah, and Dr. M. Yusuf Tanrıkulu who contributed to this thesis with their valuable comments.

I would like to also express my thanks to Dr. M. Yusuf Tanrukulu, Özgecan Dervişoğlu, Başak Kebapçı, and Selçuk Keskin for their technical assistance and valuable ideas during this study.

I also would like to thank all members of METU MEMS Center, specifically to Orhan Akar, for helping me very much in adapting the clean room working conditions.

I would like to state my thanks to Hakan Yavaş and M. Tümerkan Kesim for their technical support and intimate friendship in Materials Chemistry Laboratory.

I would also like thank to Prof. Dr. Raşit Turan for providing me the opportunity of using the GÜNAM clean room facility. I also express my thanks to Mustafa Kulakcı for his support during studies at GÜNAM facility and his companion at night experiments.

I also would like to thank to my director Dr. Hayrullah Yıldız and my manager Fahri Tamer Çukur for their support and patience during my thesis.

I also express my sincere gratitude to Erdal Kaynak for his initiative ideas and fruitful talks about physics.

I wish to thank to my friends and relatives who never stop their encouragement and always continue to motivate me.

I especially would like to thank to my mother-in-law Nilgün Ayşen Kuloğlu for her support and encouragement.

I wish to express my deepest gratitude to my parents Zübeyde Emel Karslı and Sıtkı Karslı who had endlessly and unconditionally supported me throughout my life. I am forever grateful to them for their understanding, endless patience, love, caring, and encouragement. I would especially thank my dearest physics engineer bro Kıvanç Karslı for his belief in me, support, encouragement, and providing valuable discussions.

And finally, I would like to deeply appreciate my beloved wife Ceyda Kuloğlu-Karslı for her infinite love, endless support, and motivation. Her support made it possible for me to overcome the stressful days and complete this thesis. This thesis is dedicated to her.

TABLE OF CONTENTS

LIST OF TABLES

TABLES

LIST OF FIGURES

FIGURES

CHAPTER 1

INTRODUCTION

Infrared (IR) imaging technologies have been developed rapidly in the last three decades. High performance IR detectors are now real, and they are getting better each day. However, their power consumption and cost effectiveness are major concerns for the future developments. Imaging and detection in the long wave infrared (LWIR) region, between 8 μm – 14 μm, can be achieved with photon detectors which uses direct photon excitation of electron hole pairs in narrow band gap. Photon detectors need cryogenic cooling around 77 K for high intrinsic carrier concentration. Cryogenic cooled FPAs (Focal Plane Arrays) reaches very high performances, but they are not applicable for many applications because of their heaviness and their high costs. On the other hand, uncooled (room temperature) IR detectors such as microbolometers have become the most preferred choice in most of the range of applications with their low cost. The most common applications of microbolometers are thermography, night vision for military, commercial, and automotive applications, mine detection, reconnaissance, surveillance, fire fighting, and medical imaging [1].

The working principle of microbolometer is based on the thermoresistance effect. Microbolometers absorb electromagnetic radiation which produces a temperature increase. Most commonly, this temperature change is measured by a resistance change. Microbolometer has an absorber area which absorbs incoming photons, resulting the temperature and also resistance change of the detector. This change is read by an electronic circuit.

The most common microbolometer detector active materials are VO_x, amorphous silicon, polycrystalline silicon – germanium, and yttrium barium copper oxide (YBCO). VO_x is a better bolometer material because of its combination of high TCR, good IR absorbtion characteristics and low noise [2]. It is possible to achieve high TCR values in the range of -2 %/K and -3 %/K by using VO_x active layer at room temperature [1].

There are many methods to prepare VO_x thin films, such as sputtering, pulsed laser deposition, and sol-gel method. Sol-gel method is one step forward from the others with its conspicuous features which are low cost, easiness of the process, and suitability for large area deposition [3].

Sol-gel method is a wet-chemical synthesis technique that is used primarily for the fabrication of gels, glasses, and ceramic powders starting from a chemical solution (typically a metal oxide). The sols undergo hydrolysis and condensation/polymerization reactions leading to gel networks of discrete particles or network polymers. There are two types of precursors: metal alkoxides dissolved in organic solvents (organic) or metal salts in aqueous solutions (inorganic) can be used as starting materials. Inorganic aqueous solutions are highly preferred in industrial applications because of high cost and high reactivity disadvantage of organic precursors [4]. Considering the advantages of sol-gel method, this thesis presents the vanadium oxide (VO_x) thin films elaborated by sol-gel method for microbolometer applications.

Following sections of Chapter 1 will provide an introduction about several topics. Section 1.1 gives information about the infrared region in the electromagnetic spectrum and the radiation mechanisms of the materials, while the Section 1.2 makes an overview of the infrared detectors. Section 1.3 gives the brief information about infrared detector figures of merit, and Section 1.4 discusses the microbolometer active materials and VO_x systems. Section 1.5 explains the sol-gel method and thin film coating process of sol-gels. Finally, Section 1.6 summarizes the aim of the study and the organization of the thesis.

1.1. Infrared Radiation

The infrared region, which is in the range of 0.75 μm to 1 mm, is between the visible region and the microwave region of the electromagnetic spectrum [5]. Infrared region can be divided in to five sub-regions which are near infrared, short wave infrared, mid wave infrared, long wave infrared, and extreme infrared, as summarized in Table 1.1.

Near infrared region is placed right after the visible region. Short wave, mid wave, and long wave infrared regions are the most common for infrared imaging applications. Most of the materials have emissions in these two infrared sub-regions.

Table 1.1 – Infrared Radiation Regions

Infrared Radiation Regions	Wavelength Range
Near Infrared	0.75 μm – 1.4 μm
Short wave Infrared (SWIR)	1.4 μm – 3 μm
Mid wave Infrared (MWIR)	3.0 μm – 6.0 μm
Long wave Infrared (LWIR)	6.0 μm – 15 μm
Extreme Infrared	15 μm – 1 mm

Thermal emission from an object could be in a very wide range of wavelengths in the spectrum. The range of the emission is related to the temperature of the object and the emissivity of its material. As an example, very hot metal rod has thermal emission at visible region. It shines mostly red which is the closest sub region of visible region to the infrared region. If the metal rod is extremely hot it shines in white color which is the mixture of the visible region. However, if the same metal rod is at lower temperatures there is not any emission in the visible range. It has emission at higher wavelength regions. To be able to see object, the radiation should

be reflected or emitted from that object. As it was explained, the emission is related to the temperature of the object.

As can be seen in the Figure 1.1 the incident radiation can be reflected, absorbed, and transmitted from an object. Emitting radiation is a result of an internal motion of the object. The relation between these radiation mechanisms can be written as;

$$\alpha + \rho + T = Incident \tag{1.1}$$

where α is the absorbed radiation, ρ is the reflected radiation and T is the transmitted radiation. The sum of these radiations is equal the incident radiation.

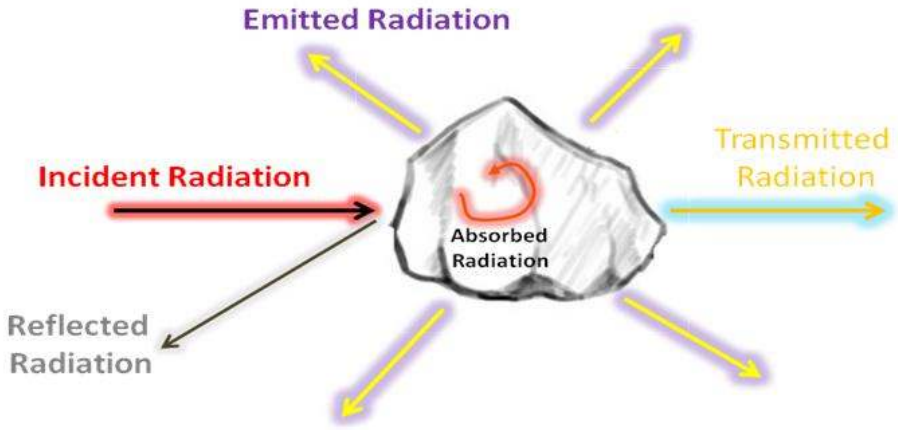

Figure 1.1– Radiation mechanisms; when the incident radiation reaches the material, it can be absorbed, transmitted or reflected. The emitted ration is the consequence of the internal motion of the material.

Human eye has an ability to see the radiation which is in the visible range. In day light, human eye can see most of the objects by the reflection of the sun light from the objects. At night (no illumination), it is only possible for humans to see the radiation which is emitted from the objects. Thermal radiation sensors can sense the radiation in the infrared region which can not seen by human eye.

All the materials which have temperature above the 0 K radiate in the infrared region. However atmosphere only let the some parts of the infrared radiation pass through it. These allowed windows are known as 3 μm to 5 μm MWIR and 8μm to 14 μm LWIR regions. As it is seen from the Figure 1.2 that only some part of the radiation can pass, the others are absorbed by the molecules in the atmosphere.

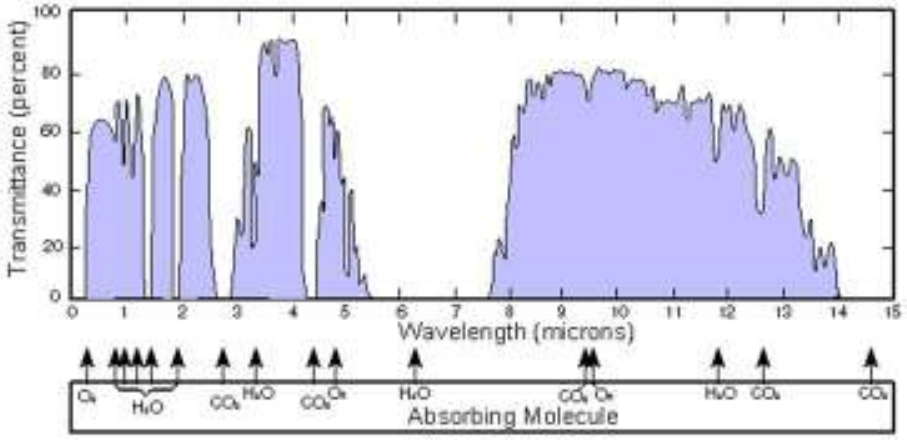

Figure 1.2 – Plot of atmospheric transmittance in part of the infrared region [6].

Thermal radiation sensors sample the incoming radiation and produce an electrical signal proportional to the total radiation that reaches the detector surface.

1.2. Infrared Detectors

Thermal radiation sensors simply enable visualization/imaging in the dark. There are many military and commercial imaging applications based on thermal radiation sensors. There are two types of detectors that can sense the incoming infrared radiation. One of them is photon detectors and the other is thermal detectors.

1.2.1. Photon Detectors

The working principle of photon detectors is straight forward. The incoming infrared photons generate electron hole (e-h) pairs which are collected by a circuit. Incoming

photons should have higher energy than the energy band gap (E_g) of the detector material to generate e-h pairs. However, these detectors are suffered from thermal noise. As it seen in the Figure 1.3.b most of the electrons are in the conduction band at room temperature, so it is difficult to sense the e-h pair which is generated by an incoming photon.

Photon detectors should be cooled down to lower temperatures with cryogenic coolers to keep most of the electrons in valance band while there is no illumination. Figure 1.3.a shows the band gap structure of a semiconductor which is at low temperature.

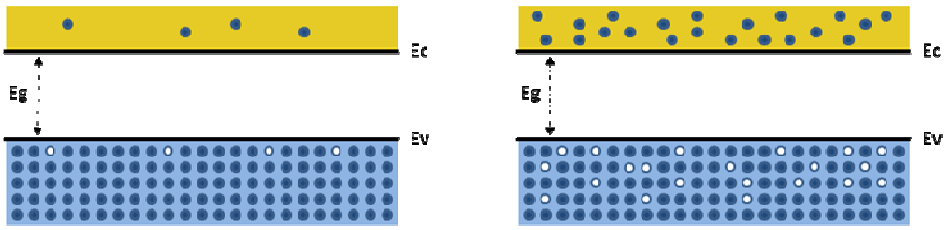

(a) (b)

Figure 1.3 – Band gap structure of a semiconductor (a) at low temperature (b) at room temperature, E_v refers valance band, E_c is conduction band, and E_g is the band gap of the semiconductor.

Response of the photon detectors are very fast, because while the photon reaches the detector an electron hole pair is generated immediately. They have very high sensitivities. However, the production processes of the photon detectors are complicated and expensive. They consume much power and their life time is very limited compare to thermal detectors.

1.2.2. Thermal Detectors

The other type of infrared detectors is thermal detectors which absorbs the incoming infrared radiation and respond with a change of an electrical property such as resistance, capacitance or voltage. This electrical change is measured by an electronic read out circuit. Response time of the thermal detectors is longer than the photon detectors because they need a heat up time after the incoming radiation is absorbed. Thermal detectors work at room temperature. Their production is easier than photon detectors. They are less expensive; consume less power and smaller in size compare to photon detectors. There are three most common thermal detectors; thermoelectric detectors (thermopiles), pyroelectric detectors and resistive microbolometers.

1.2.3. Thermoelectric Detectors (Thermopiles)

Thermoelectric detectors work on the principle of seebeck coefficient difference of two materials. Two different electrically conducting materials are joined together at a hot junction. Figure 1.4 shows the thermocouple structure.

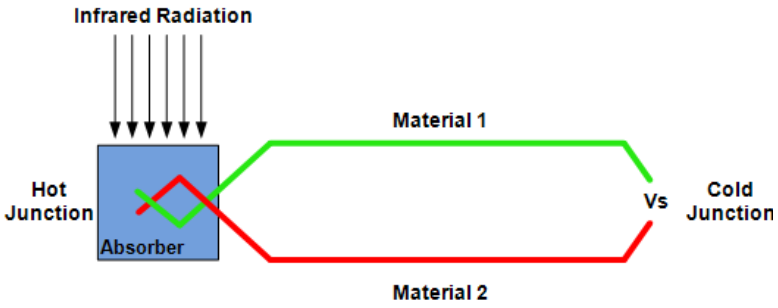

Figure 1.4 – Thermocouple structure, two materials with different seebeck coefficient.

Hot junction absorbs the incident radiation while the cold junction is shielded. Temperature difference between hot junction (detecting junction) and cold junction

(shielded junction) create a voltage difference between two materials [7]. This structure is called as thermocouple. Obtained voltage is directly related to temperature difference between the junctions and the electrical conductivity of the materials.

Obtained voltage can be written as

$$V_s = (S_1 - S_2)\Delta T \tag{1.2}$$

where V_s is the thermoelectric signal voltage, S_1 and S_2 are the seebeck coefficients of the materials and ΔT is the temperature difference between hot junction and the cold junction.

To achieve higher thermoelectric signal voltage, thermopile structure is created with connecting a series of thermocouples. Figure 1.5 shows a thermopile structure which is created by connecting a series of thermocouples.

$$V_s = N(S_1 - S_2)\Delta T \tag{1.3}$$

where N is the number of thermocouples on a thermopile structure [8].

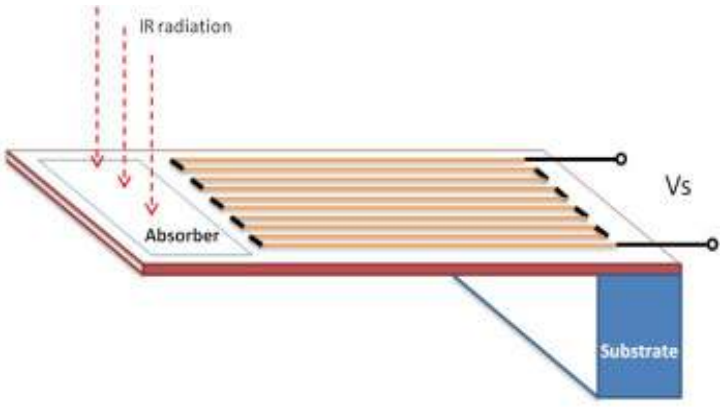

Figure 1.5 – Basic structure of a thermopile, N thermocouples are connected to obtain higher voltage difference between two different materials.

There is no need to biasing the thermopile circuit, so detector performance does not affected from any 1/f noise and no bias induced heating occurs. They have linear response in wide range of temperature, so they are good candidates for temperature measurements. They are less expensive than other detectors. However, thermopiles have limited performance and small responsivities [9]. They have moderate Noise Equivalent Temperature Difference (NETD) values. Pixel size of a thermopile is very large compare to other thermal detectors; it is why the detector arrays are small [10].

1.2.4. Pyroelectric Detectors

Potential difference between opposite faces of pyroelectric materials is detected due to spontaneous internal electrical polarization change. Figure 1.6 shows the temperature dependency of the polarization change. The amount of the polarization depends on permittivity and dielectric features of the material [7].

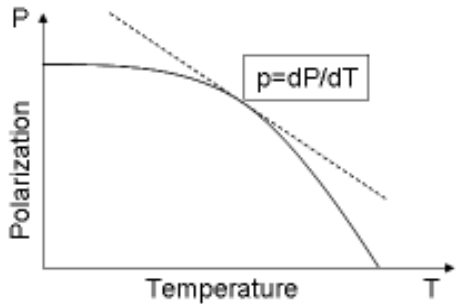

Figure 1.6 – Pyroelectric effect can be described with this polarization-temperature curve.

The potential difference between the opposite faces of the material generates a transient current which is flow through an external circuit. Figure 1.7 shows the basic structure of a pyroelectric detector.

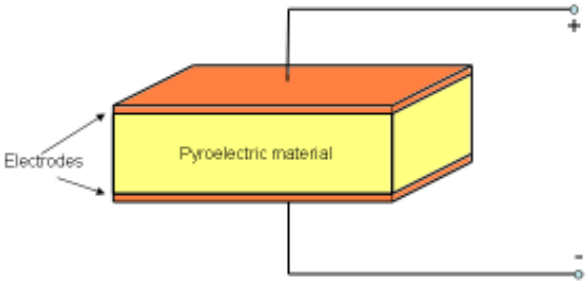

Figure 1.7 – Basic structure of a pyroelectric detector which has pyroelectric material between two electrodes.

The magnitude of the transient current is given by;

$$I_s = pA\frac{d(\Delta T)}{dt} \tag{1.4}$$

where A is the pixel active area, p is the pyroelectric coefficient. Pyroelectric effect disappears at the temperature called as Currie temperature. Pyroelectric detectors have high responsivity relative to the thermoelectric detectors. However, a chopper should be used for the pyroelectric detector applications.

1.2.5. Resistive Microbolometers

The working principle of microbolometers is the resistance change due to the temperature change by the absorption of IR radiation. IR active area absorbs the incident radiation; the resistance change is detected by bias current and voltage change measured.

One of the main characteristics of the microbolometers is surface micromachining techniques used to build the structures [9].

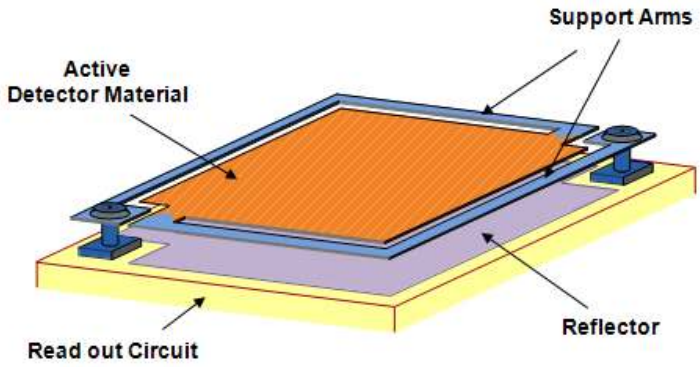

Figure 1.8 – Example of microbolometer pixel structure.

Microbolometers are more expensive than thermopiles much cheaper than cooled photon detectors. Their response time is longer than photon detectors due to the heat up time [11]. Detectors are starring array so the electrical bandwidth is much lower than scanned photon detectors. They can operate at room temperature, there is no need to cool down these detectors. They consume less power than photon detectors and their operation duration is relatively longer than photon detectors [9].

Performance of the detector is dependent on geometrical and optical design, focal plane array manufacturing techniques, quality of isolation, read out integrated circuit (ROIC) and intrinsic properties of temperature sensing material [1]. Figures of merit that are used to determine the performance of the infrared detectors are discussed in the following section.

1.3. Figures of Merit

The analysis of all types of thermal IR detectors begins with a heat flow equation that describes the temperature increase in terms of the incident radiant power [12]. IR detector figures of merit are briefly described in the following subsections.

1.3.1. Temperature Sensitivity

Temperature sensitivity is a parameter that describes the temperature dependency of uncooled detectors. For resistive type microbolometers it is the temperature dependence of the resistance. The resistance of the detector change with the increase or decrease of the temperature. This dependence can be described as temperature coefficient of resistance (TCR).

$$\alpha = \frac{1}{R}\frac{dR}{dT} \tag{1.5}$$

where α is the TCR of the detector, R is the resistance at the temperature T. The TCR is a property of the active material. The active material can be metal or semiconductor. If the material is metal the TCR is positive, and if the material is semiconductor the TCR is negative.

The free carrier concentration of the metals does not change so much with the change of the temperature. However, the mobility of the free carriers is reduced by the temperature change. The resistance of the thin film can be written as [13]:

$$R(T) = R(T_s)(1 + \alpha(T - T_s)) \tag{1.6}$$

where R(T) is the resistance dependent to temperature T, T_s is room temperature, α is TCR.

The mobile charge carriers of the semiconductors are increased with increasing temperature. Furthermore, the mobility of the carriers are increased with increasing temperature. The resistance of semiconductor thin films can be expressed as [13]

$$R(T) \propto \exp(E_g / 2k_b T) \quad i.e., \alpha = dR/RdT = -E_g / 2k_b T^2 \tag{1.7}$$

where E_g is the band gap of the semiconductor, k_b is the Boltzman's Constant.

Semiconductors such as VO_x thin films give more TCR than most metal thin films. Parameters that will be discussed in the following sections such as responsivity and detectivity are increased with the increase in TCR. However, high TCR means high

resistivity and high resistivity brings more noise and reduces the mentioned parameters [14]. For this reason the TCR, resistance, and the noise of the detector should be considered together.

1.3.2. Thermal Conductance

Microbolometers should have an isolated structure for high performance. Thermal conductance shows the level of thermal isolation of the detector. Thermal conductance is a structural performance parameter which can be changed with the design of the detector cells. Total thermal conductance of a detector can be written as

$$G_{total} = G_{s.arms} + G_{rad} + G_{environment} \tag{1.8}$$

where G_{total} is the total thermal conductance, $G_{s.arms}$ is the thermal conductance of the supporting arms of the detector, G_{rad} is the radiative thermal conductance, and $G_{environment}$ is the thermal conductance of the gas environment where the detector placed in.

Generally, radiative thermal conductance and the thermal conductance of the environment are negligible when they are compared with thermal conductance of the support arms. It is better to have lower thermal conductance to obtain better detector performance.

1.3.3. Responsivity

Responsivity is a parameter showing the amount of electrical signal output of the detector due to the incident infrared radiation received by the detector.

It is possible to find the temperature change of the detector due to the incident infrared radiation by solving the heat flow equation [15].

$$C\frac{d\Delta T}{dt} + G\Delta T = \eta P_0 e^{iwt} \tag{1.9}$$

where C is the heat capacity of the detector material, G is thermal conductance, P_0e^{iwt} is the incident infrared radiation power, w is the frequency of radiation power, and η is the absorption coefficient .

$$\Delta T = \frac{\eta P_0}{\sqrt{G^2 + w^2 C^2}} \tag{1.10}$$

Smaller C and G are required to have larger ΔT. The ratio of thermal capacitance and thermal conductance can be expressed as thermal time constant. ΔT can be written in terms of thermal time constant as follows.

$$\Delta T = \frac{\eta P_0}{G\sqrt{1 + w^2 \tau_{th}^2}} \tag{1.11}$$

Output of detector can be expressed in terms of voltage or current due to the read out design. The change of the output due to the temperature change can be written as following equations.

$$\Delta V = I_{bias} \Delta R = I_{bias} \alpha R \Delta T \tag{1.12}$$

$$\Delta I = \frac{V_{bias}}{R} - \frac{V_{bias}}{R - \alpha R \Delta T} \approx -\frac{V_{bias}}{R} \alpha \Delta T \tag{1.13}$$

where I_{bias} is the bias current of the detector, R is the detector resistance, α is the TCR of the detector and if the detector is biased with voltage, V_{bias} is the bias voltage of the detector, ΔT is the temperature change.

The resposivities for the voltage biased and current biased detectors are expressed as [16].

$$R_v = \frac{I_{bias} \alpha R \eta}{G\left(1 + w^2 \tau_{th}^2\right)^{1/2}} \tag{1.14}$$

$$R_i = \frac{V_{bias} \alpha \eta}{RG\left(1 + w^2 \tau_{th}^2\right)^{1/2}} \tag{1.15}$$

Responsivity is proportional to TCR and inversely proportional to thermal conductance. The detector material and the isolation of the detector are the primary focus for responsivity of the detector.

1.3.4. Noise Equivalent Power (NEP)

The amount incident power required to produce a signal which is above the noise level of the detector. The signal power should be higher than the noise level to detection.

$$NEP = \frac{V_{noise}}{R_v} = \frac{i_{noise}}{R_i} \tag{1.16}$$

where R_v and R_i are the responsivity and V_{noise} and i_{noise} are the total rms noise voltage and current.

There are four major noise mechanisms in bolometer [8].

a) Johnson (Thermal) Noise
b) 1/f Noise
c) Temperature Fluctuation Noise
d) Background Fluctuation Noise

Johnson noise is the fluctuation due to the thermal motion of charge carriers in resistive materials and occurs in the absence of electrical bias.

$$i_{n,johnson} = \sqrt{\frac{4kT\Delta f}{R}}, \quad V_{n,johnson} = \sqrt{4kTR\Delta f} \tag{1.17}$$

where k is the Boltzman constant, T is the temperature in Kelvin, R is the resistance of the detector, and Δf is the bandwidth.

1/f noise is found in semiconductors. 1/f noise is a major problem at low level frequencies and inversely proportional to square root of frequency.

$$V_{n,1/f} = \sqrt{\frac{V^2 n}{f}} \tag{1.18}$$

where V is the bias voltage, n is the 1/f noise parameter, f is the frequency. 1/f noise depends on the active bolometer material [12].

Temperature fluctuation noise is caused by the change of the detector temperature due to the heat loss from detector to detector surroundings.

$$V_{n,tf} = \sqrt{\frac{4kTG}{\eta}} R_v \tag{1.19}$$

where G is the thermal conductance, η is the absorption coefficient, and R_v is the responsivity of the detector.

Background fluctuation noise is caused by the random changes of incoming radiation power and the random changes of emitted power from the detector. It can be expressed as.

$$V_{n,bf} = \sqrt{8A_d \eta \sigma k \left(T^5_{bolometer} + T^5_{background}\right)} R_v \tag{1.20}$$

where A_d is the detector area, η is the absorption coefficient, σ is the Stefan-Boltzman constant, k is the Boltzman constant, $T_{bolometer}$ and $T_{bacground}$ are the temperatures of bolometer, and the background, R_v is the responsivity of the detector.

Total rms noise voltage written as,

$$V_{n,total} = \sqrt{V^2_{n,jhonson} + V^2_{n,1/f} + V^2_{n,tf} + V^2_{n,bf}} \tag{1.21}$$

1.3.5. Noise Equivalent Temperature Difference NETD

NETD is an infrared imager performance parameter which has dependency not only the detector but also the other parts of the imaging system such as optics.

$$NETD = \frac{4F^2 V_n}{\tau A_d R_v \left(\Delta P / \Delta T\right)_{\lambda_1 - \lambda_2}} \tag{1.22}$$

where, F is the focal ratio of the optics, τ is the transmittance of the optics, $(\Delta P/\Delta T)_{\lambda 1-\lambda 2}$ is the change in power per unit area radiated by scene at temperature T, T is measured within the spectral range of λ_1 to λ_2.

1.3.6. Detectivity (D*)

Detectivity is a parameter that is needed for comparison of different detectors in terms of performance. It is possible to compare different pixel size different scanning rate imagers with detectivity.

$$D^* = \frac{\sqrt{A_D \Delta f}}{NEP} = \frac{\sqrt{A_D \Delta f}}{V_n} R_v \tag{1.23}$$

where A_D is the active detector area, Δf is the bandwidth of the system, NEP is the noise equivalent power of the detector, R_v is the voltage responsivity of the detector and V_n is the total rms noise voltage.

TCR and 1/f noise are the microbolometer active material dependent performance parameters. The choice of the active material directly effects the performance of the detector. Microbolometer active materials will be briefly explained in the following section.

1.4. Microbolometer active materials

Microbolometer active material has a crucial importance on the performance of the infrared imaging devices. The active material determines the sensitivity of the microbolometer. Active material features that resistance, TCR, and 1/f noise are the most effecting parameters on the detector design. The read out compatibility of the material is also a very important issue. There are various processing routes for developing active material on the detector structure in the form of a thin film. However, some techniques such as high temperature deposition are not compatible with the ROIC of the detector. Contacts of the circuit can melt at high temperatures during deposition of the sensing material.

Briefly, TCR shows the response of the material due to temperature change, resistance is the critical parameter for the appearing noises and designed resistor value of the detector; 1/f noise is material dependent characteristic parameter and the material should compatible with the read out circuit. However, simple thin film coating step for the active material is still a technological challenge.

Table 1.2 – Desired Features of Resistive Microbolometer Sensing Material

Resistive Microbolometer Sensing Material Features	
TCR	High
Resistance	Low
1/f	Low
ROIC Compatible	OK

There is a wide variety of materials used as microbolometer active material. Vanadium oxide (VO_x), poly-Silicon-Germanium (Poly Si-Ge), amorphous Silicon (a-Si), and YBaCuO are the most widely used detector materials. Main characteristics of these materials can be briefly stated as follows.

VO_x has high TCR values around -2 %/K at room temperature. VO_x can be in many different states such as VO_2, V_2O_5, V_2O_3. It is the most common microbolometer sensing material. There are various deposition techniques of VO_x such as sputtering, pulsed laser deposition, and sol-gel method [1, 17].

Poly Si-Ge has very low thermal conductance. It is possible to produce very thin membranes. However, when the poly Si-Ge is deposited on substrates by chemical vapor deposition it requires relatively high temperatures above 650 °C [18].

a-Si can be produced by common silicon fabrication techniques. Amorphous silicon has silicon fabrication compatible process. No phase transformation occurs while the temperature is changing which means that resistance continuously decreases with increasing temperature. It is possible to produce very thin membranes which also

lower the thermal conductance. Amorphous silicon can be deposited at very low temperatures [1].
YBCO can be deposited at room temperature. It is possible to achieve high TCR values around 3 %/K – 4 %/K with this material. YBCO has low 1/f noise [1].

1.4.1. VO_x as Microbolometer Active Material

VO_x is a suitable bolometer active material because of its combination of high TCR, good IR absorption characteristics, and low 1/f noise. It is possible to achieve high TCR values in the range of -2 %/K and -3 %/K by using VO_x active layer at room temperature. VO_x can be deposited by sputtering, pulsed laser deposition, and sol-gel method.

The material used as the detector active material must provide significant changes in resistance in response to temperature change. Using a material with low room temperature resistance is also important. Lower resistance across the detecting material mean less power will need to be used. Also, there is a relationship between resistance and noise, the higher the resistance the higher the noise. Thus, for easier detection and to satisfy the low noise requirement, resistance should be low [19].

Vanadium is a multivalent element and can be in different oxidation states. A variety of vanadium oxide phases, V_2O_5, VO_2, V_2O_3, and multiphase V_xO_y combinations have been used as active material in microbolometer applications. The important question is "which one of them or which combination of them gives the better performance results as a microbolometer active material?"

VO_2 has low resistance but undergoes a metal-insulator phase change near 67 ºC and also has a low value of TCR. On the other hand, V_2O_5 offers high resistance and also high TCR. Many phases of VO_x exist although it seems that ($x \approx 2 – 2.3$) VO_x phases have become the most popular for microbolometer applications [20, 21]. Brief information about vanadium oxide systems will be given in the following section.

1.4.2. Vanadium Oxide Systems

Vanadium is a transition metal with the symbol V. There are more than fifteen stable vanadium oxide phases. The common oxidation states of vanadium are V^{2+} in VO, V^{3+} in V_2O_3, V^{4+} in VO_2, V^{5+} in V_2O_5. V_2O_5 is the highest oxygen state of vanadium oxygen systems. There are V_4O_9 V_6O_{13}, and V_3O_7 intermediate states between V_2O_5 and VO_2. The intermediate phases called Magnéli Phases are between the VO_2 and V_2O_3.

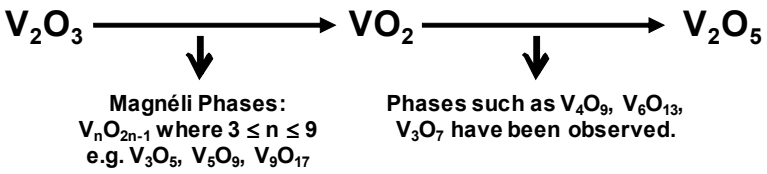

Figure 1.9 – Major oxidation states and the other intermediate states of vanadium oxide.

The phase diagram of vanadium oxygen is given in Figure 1.10. As depicted by the diagram, there are three thermodynamically stable single phase fields of VO_x which are VO_2, V_6O_{13}, and V_2O_5 at around this rate.

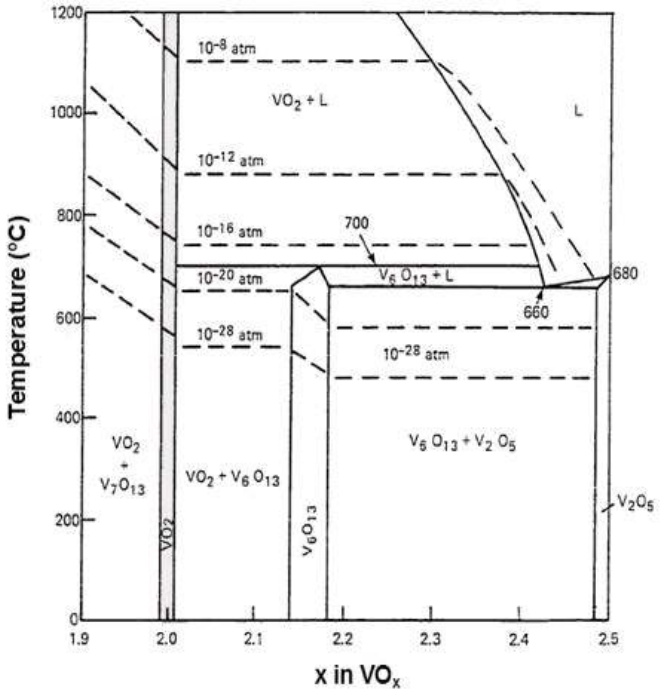

Figure 1.10 – Phase diagram for the vanadium oxygen system [3].

Many oxygen phases of the vanadium display structural phase transition (Table 1.3). VO_2 has a phase transition at 67 °C (340 K).

Table 1.3 – Metal – insulator transition temperatures of different vanadium oxide phases.

Oxide Phase		Transition Temperature (K)
V_2O_3		**155**
Magnéli Phases	V_3O_5	430
	V_4O_7	238
	V_5O_9	135
	V_6O_{11}	170
	V_7O_{13}	---
	V_8O_{15}	68
	V_9O_{17}	79
VO_2		**340**
V_6O_{13}		150
V_2O_5		**530**

There is an interest on thin film processes of vanadium oxides in literature, due to their widespread applications. There are many possible ways of thin film growth method of vanadium oxide. Chemical vapor deposition (CVD), sputtering, pulsed laser deposition, epitaxial growth and sol-gel method are the most common thin film preparation of vanadium oxides. Sol-gel method and thin film coating will be discussed in the following section.

1.5. Sol-Gel Method and Thin Film Coating

Beside the all other thin film preparation methods, sol-gel method has many advantages. It does not require a high vacuum systems and the instrumentation is much simpler. High purity stoichiometry can be achieved by low temperature processes. Large substrates can easily be coated. It allows high deposition rates. The starting materials are mixed on a molecular level; a very good chemical homogeneity can be obtained [22].

1.5.1. Sol-gel Chemistry

Vanadium is a transition metal. A vanadium solution can be prepared from inorganic (salts) or organic (metal-alkoxide) precursors. Alkoxides contain organic groups with negatively charged oxygen atom which stabilizes the transition metal with its electro negativity.

Organic sol-gel preparation method, involving use of alkoxide precursors and organic solvents, has several advantages. Multi component films can be prepared by mixing several metal-alkoxides in the same solvent. In addition, highly homogeneous and products with molecular level purity can be obtained. However, organic sol-gel processes are quite expensive than inorganic sol-gel processes and highly reactive [4, 22, 23]. It is possible to say that inorganic sol-gel preparation methods are more appropriate for industrial applications.

Inorganic precursors formed by dissolution of metal salts in aqueous, such as water. Main mechanism of this dissolution is the charge transfer from water molecule to the empty orbitals of the transition metal [24]. Hydrolysis of inorganic salt defined as:

$$[M(OH_2)]^{z+} \rightarrow [M\text{-}OH]^{(z-1)+} + H^+ \rightarrow [M{=}O]^{(z-2)+} + 2H^+ \qquad (1.24)$$

where M is the transition metal. Different types of ligands can be formed in the solution in respect to molar ratio of the hydrolysis.

- Aquo: M-(OH_2)
- Hydroxo: M-OH
- Oxo: M=O

Condensation which is also known as polymeration, is described as formation of one big molecule from two molecules and a small molecule is removed. Mostly the removing molecule is H_2O. Condensation is occurred in two ways which are olation and oxolation in inorganic precursors. The olation and oxolation mechanisms are shown in the Figure 1.11.

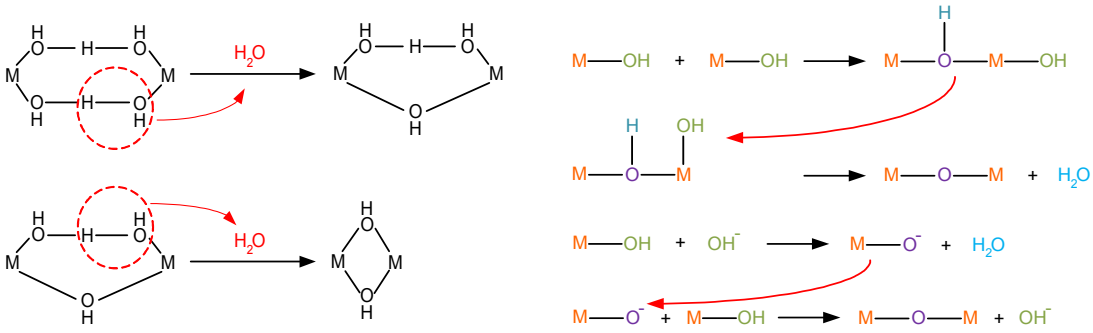

Figure 1.11 – Olation (left) and oxolation (right) condensation mechanisms.

1.5.2. Thin Film Coating

There is various thin film coating techniques applicable to the sols. Spin coating, dipping, and spraying are the major coating techniques. Spin coating and spraying are used to obtaining coatings on only one side of a substrate material. Due to its easiness and controllability, spin coating technique is mostly used for one sided coating deposition.

The spin coating starts with the deposition of the sol on to the wafer. The spin coater starts to spin up and the solution covers the whole surface of the wafer. In spin off phase, maximum spinning speed is achieved and the solution starts to get thinner like a sheet on a table. At the last phase of the spin coating evaporation is occurred. Figure 1.12 shows the illustration of spin coating steps.

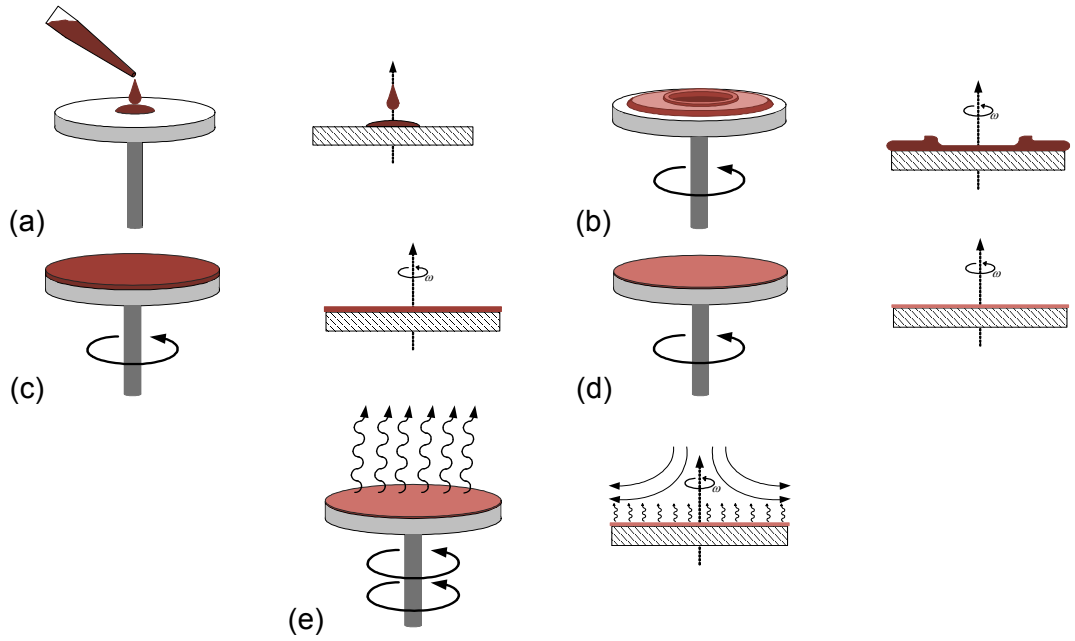

Figure 1.12 – (a) deposition (b) spin up (c) spin off phase-1 (d) spin off phase-2 (e) evaporation.

Spraying is the other common one sided coating method. The coating solution is sprayed on to the surface of a substrate. It is difficult to control the homogeneity of the film thickness during spraying.

Dipping is a two sided coating method for sol applications. The substrate is dipped in to the sol and then removed from the sol to outside of the sol containing cup. The excess of the sol is dropped and evaporation occurs. Figure 1.13 shows the Dip coating process steps.

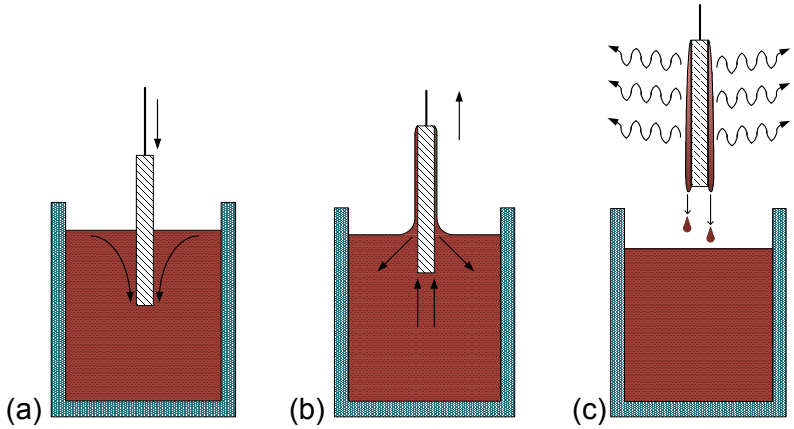

Figure 1.13 – Dip coating processes steps (a) dipping (b) wet layer formation (c) Solvent evaporation.

1.6. Organization of the Thesis

The objective of this study is to obtain a VO_x thin film with high TCR, low resistivity, and low 1/f noise for microbolometer applications. VO_x, the active material of the detector, was prepared by sol-gel method using inorganic vanadium precursor. Spin coating was used to prepare thin film active material layer on the silicon and silicon nitride wafers. Different oxygen states of VO_x were achieved with different reducing atmosphere annealing processes. The coating sol and annealed thin films were initially characterized by using Thermo-Gravimetric Analysis (TGA), X-Ray Diffraction (XRD), and viscosity of the coating sol and the

thicknesses of the thin films are also measured. The performance parameters of the VO_x active layer such as sheet resistance, TCR, and noise were measured to verify the quality of the developed VO_x layers for their use in microbolometers.

Chapter 2 gives literature review about sol-gel processing of vanadium oxide thin films. It also highlights the experimental method, in regard to sol-gel procedure and related results on the properties of VO_x thin films.

Chapter 3 gives literature review about post coating annealing step for achieving different states for VO_x thin films. It also explains the annealing procedure, results of successfully coated VO_x thin films.

Chapter 4 gives the performance results of the successfully coated and annealed thin films. The performed examinations include sheet resistance, TCR, and noise measurements.

Finally, Chapter 5 summarizes the results of this thesis study.

CHAPTER 2

SOL-GEL DEPOSITION OF VO_x THIN FILMS

There are many methods to prepare VO_x thin films, such as reactive sputtering, pulsed laser deposition, vacuum evaporation, and sol-gel techniques [25-29]. Low cost, easiness of the process, low processing temperatures, suitability for large area deposition and very pure products (crystallization, distillation, electrolysis) are the most remarkable features of the sol-gel method [3, 4, 24, 30 , 31].

Due to these advantages of the sol-gel process, this method is chosen for this study to prepare VO_x microbolometer active material. Section 2.1 gives information about the preparation trials of sol-gel vanadium oxide in the literature. Section 2.2 describes the sol preparation and thin film coating procedures. Section 2.3 summarizes the results of the sol preparations and thin film coating processes.

2.1. VO_x Sol-Gel Trials in the Literature

There are various ways to prepare a metal oxide solution for thin film coating. As mentioned earlier, organic and inorganic are two different sol-gel preparation methods. Both of these methods can be used for VO_x sol-gel preparation. Various VO_x sol-gel preparation methods have been described in the literature.

2.1.1. Organic VO_x trials

The main route for organic VO_x solution preparation method is described by Livage [32] as follows:

Vanadium alkoxides $VO(OR)_3$ ($R=OPr^i$, OAm^t) were prepared by heating the mixture ammonium vanadate and alcohol in an nonpolar solvent (C_6H_{12}). The reaction can be written as

$$NH_4VO_3 + 3ROH \rightarrow VO(OR)_3 + 2H_2O + NH_3 \quad (2.1)$$

Reduced pressure was used to purify the resulting alcohol and it was dissolved in its parent alcohol [33]. Due to the disadvantages which were mentioned in Section 1.5.1 of organic sol-gel method, inorganic sol-gel process of vanadium oxide was mostly preferred instead of organic sol-gel process. Inorganic sol-gel trials will be examined in the following section.

2.1.2. Inorganic VO_x trials

Takahashi reported that it is possible to make polyvanadate by solving metallic vanadium powder in hydrogen peroxide [25]. When metallic vanadium powder is dissolved in hydrogen peroxide in ambient conditions, highly exothermic reaction occur leading to violent conditions [25, 32]. Therefore, an external cooling device such as ice cooled bath can be used to decrease the violence of the reaction [25]. However this type of external cooling hampers the dissolution of the metal in the H_2O_2. In the absence of external cooling, vanadium can be dissolved in hydrogen peroxide in 30 min, however external cooling expands this process to 5 h – 6 h. After all the vanadium is dissolved in the H_2O_2 the solution is taken to rest to increase the solution temperature to the ambient temperature. An exothermic and less violent reaction was occurred while the temperature of the solution increases. Instead of leaving the solution to rest, It is possible to heat the solution to higher temperatures (close to ambient temperature ~ 50 °C) [25]. More rapid reaction is occurred if the solution is heated.

Concentration of the hydrogen peroxide can also change the reaction characteristics. If the concentration of the hydrogen peroxide is kept at lower levels (around 10 %), exothermic reaction is not violent [32].

Kudo and his colleagues (Tetsuichi Kudo team) used the following solution preparation formula in their experiments.

> Metallic Vanadium (powder) + 30 % H_2O_2 → Polyvanadate – clear brown color (the ratio of H_2O_2/Vanadium powder = 30 ml / 0.3 g) in ice cooled bath [25, 34]

Ugaji and Hibino (Tetsuichi Kudo team) reported the following formulation and steps of their solution preparation process [35 - 37].

> Metallic Vanadium (powder – 325 mesh purer than 99.5 %) + 30 % H_2O_2 → Clear brown solution (in ice cooled bath) → Drying in evaporator at 35 °C → dark brown powder $V_2O_5 \cdot nH_2O$ (n is 1.6~2.3)

Instead of using vanadium powder, pure V_2O_5 can be used to obtain $V_2O_5 \cdot nH_2O$.

Alonso, Livage, and Wang used the following formula while preparing their samples and they observed the following steps in their experiments [32, 38, 39].

> V_2O_5 + H_2O_2 10 % →Clear orange solution (after ten minutes – oxygen release continues slowly) → Deep red solution (after 2 hours) → Orange-yellow solution (oxygen release stops) → deep red flocculated system (after a few hours) →homogeneous viscous dark red gel (after 24 hours) → $V_2O_5.nH_2O$ xerogel ($n \approx 2$)

Fontenot reported that they used H_2O_2 and V_2O_5 to prepare such materials [40]. Their preparation method is summarized below:

> 30 % H_2O_2 +DI Water + V_2O_5 → 0.1M Peroxovanadate (the ratio of $H_2O_2/V_2O_5 \sim 8$) at 25 °C

> 30 % H_2O_2 + V_2O_5 → 0.5 M Peroxovanadate (the ratio of $H_2O_2/V_2O_5 \sim 25$) at 5 °C

Another method with V_2O_5 powder was reported by Dachuan and also by Ningyi. Instead of solving the V_2O_5 in H_2O_2, they melted the V_2O_5 [26, 41 - 43].

V_2O_5 (melted at 900 °C) + DI Water (at 20 °C) → Brownish V_2O_5 solution

V_2O_5 (melted at 800 °C – 1100 °C) + DI Water (at 20 °C) → Brownish V_2O_5 solution [42]

Many inorganic vanadium solution preparation techniques are used in the literature. The appropriate method can be chosen from these methods. Solution preparation and thin film coating procedures that are used in this study will be described in the following section.

2.2. Solution Preparation and Thin Film Coating Procedures

In this study, coating solutions were prepared by mixing DI water and vanadium solid material which was the dried product of dissolution of vanadium powder and hydrogen peroxide. The thin films were prepared by spin coating the coating solution on Si or SiN_x substrates. As it was mentioned above the coating solution was prepared by mixing a vanadium base solid material and DI water. The preparation details of solid material preparation, coating solution preparation, and spin coating procedures will be described in following subsections.

2.2.1. Solution Preparation Procedure

2.2.1.1. Solid Material Preparation (Vanadium)

The first step of preparation of coating solution is to obtain a solid material. The preparation of solid material was started by dissolving metallic vanadium powder (powder, 325 Mesh purer than 99.5 %) in an iced cooled 30 % H_2O_2. After the process, bright reddish solution is obtained. The ratio of vanadium powder to hydrogen peroxide is 1 g : 100 ml. Figure 2.1 shows the flow diagram of this step.

Vanadium powder + H_2O_2 (1 g : 100 ml) → Bright reddish color solution

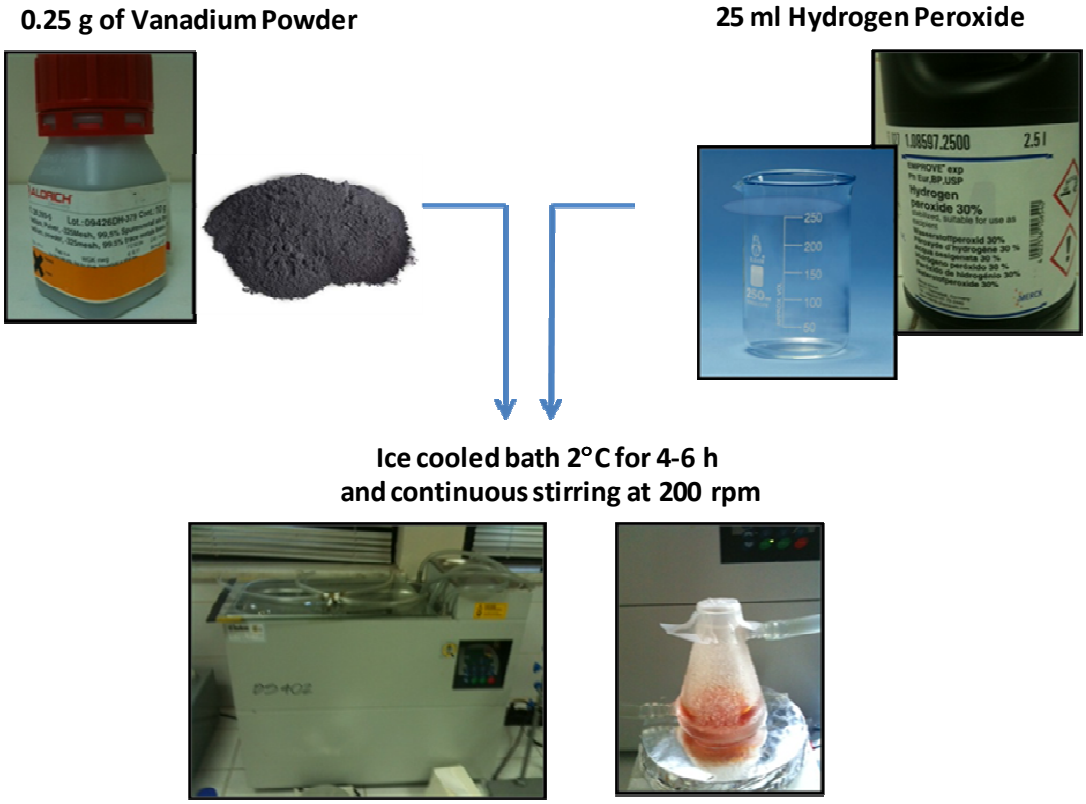

Figure 2.1 – The flow diagram of first step of the solution preparation. Appropriate amount of vanadium powder and hydrogen peroxide were mixed in ice cooled bath for 4-6 hours.

In ambient, an exothermic and violent reaction occurs, when the vanadium powder is added to hydrogen peroxide. To prevent this violent reaction dissolving process is done in an ice cooled bath. The solution is kept in iced cooled bath and stirred with magnetic stirrer (150-200 rpm) until all the vanadium powder dissolved in hydrogen peroxide. Ice cooled bath provides controllable reaction. However, when an ice cooled bath is used, the experiment duration becomes very long compare to the experiment which is done in ambient conditions. Dissolving duration varies between 4 hours to 6 hours when the dissolution done in iced cooled bath. As shown in the Figure 2.2, the color of the solution changes by the time and it becomes bright reddish at the end of the process. The color change of the solution is indicating that the vanadium powder is solved in hydrogen peroxide.

(a) (b)

Figure 2.2 – (a) Vanadium - hydrogen peroxide mixture in iced cooled bath (2 ºC)in the beginning of the dissolution process. (b) light red color mixture after a couple hours (4 hours – 6 hours).

The solution is removed from iced cooled bath after assuring that all the vanadium powder is dissolved. It can be kept at room temperature or in a hot (50 °C) water bath. The reaction time decreases when the solution was put in to a hot water bath. An oxygen release reaction is occurred at the end of the process. Highly exothermic decomposition of hydrogen peroxide reaction is occurred. Figure 2.3 shows the moments of this exothermic decomposition.

Violent bubbling of oxygen occurs during the reaction. Oxygen release rate gets higher by the time, after the sol is taken to the rest. The amount of oxygen release is increase with time till the higher rate of oxygen release (violent bubbling) occurs. The bubbling occurs in 30 minutes to 60 minutes in ambient or in 2 minutes in hot water bath and then oxygen release suddenly stops. The temperature of the solution is higher than room temperature when the reaction is stopped.

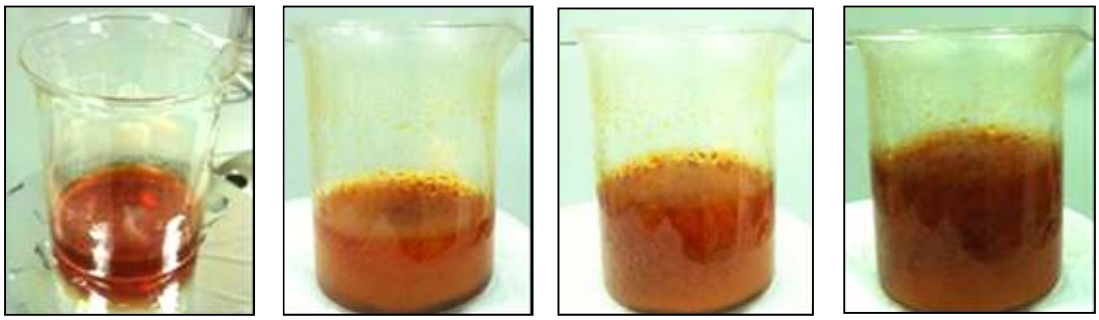

Figure 2.3 – (a) The solution was in rest in ambient condition (at the beginning), (b) Oxygen release was reaching the peak point (c,d) Violent bubbling.

The oxygen release of the decomposition reaction given as follows:

$$VO_X + nH_2O_2 \rightarrow VO_X \cdot nH_2O + \frac{n}{2}O_2 \qquad (2.2)$$

After this exothermic reaction finishes, in other words oxygen release stops, clear, homogeneous, and very light orange color solution was obtained. However, as seen in the Figure 2.4, flocculation which is a process colloids come out of suspension in the form of floc or flakes starts in 5 minutes. If this flocculated solution remove to rest in ambient conditions it stars to swell and gelation occurs.

Figure 2.4 – (a) Homogenous red sol at ambient temperature right after the reaction is stopped, (b) Dark brown sol with particles at the bottom (Flocculation).

However, decomposition reaction of hydrogen peroxide is not controllable, so the features of the final product of such gel like solution differ for every trial. To control the homogeneity, viscosity, and the amount of the solution, the flocculated solution is put into oven at 80 °C for 24 hours to achieve a solid material. Figure 2.5 shows the moments of the drying process of the sol. Figure 2.6 shows final product of this drying process.

(a) (b)

Figure 2.5 – Top view from the drying cup (a) after 12 hours the material does not dry, it is not liquid also (b) after 24 hours it becomes solid.

Figure 2.6 – The solid material obtained after 24 hours drying process.

To understand the features of the solid material, it is characterized by XRD and TGA. As shown in Figure 2.7, the solid material is powdered by pounding in a

mortar. The purpose of powdering the material is to increase the surface area of the sample which was going to be annealed for characterization.

Figure 2.7 – The solid material pounded in a mortar and powdered for characterization processes.

The annealing is applied at 370 °C for 2 hours. After annealing the difference between the annealed sample and the not annealed sample is observed by visual inspection, XRD, and TGA. XRD and TGA were done to both annealed and not annealed solid material samples. The XRD measurements were performed for 2θ of 10° to 70°. TGA was performed under air and nitrogen environments between 25 °C and 550 °C.

TGA is applied to the samples to determine their weight-temperature relation. The weight of the sample can be change with the change of temperature by any reaction such as one of the components of the sample decomposes into a gas.

XRD is performed for phase analysis.

2.2.1.2. Coating Solution Preparation

The solid material is solved in DI water to obtain the final coating solution. The mixing ratio of solid material to DI water is varied between 1 mg : 50 ml to

1 mg : 25 ml. The density and the viscosity of the coating solution are directly dependent on the mixing ratio. It is possible to obtain better coatings with more viscous and dense solutions. However it is became more difficult to solve all the solid particles in the mixture. Those particles create cracks and discontinuities on the thin film. Better coating results were achieved between the ratios of 1 mg : 30 ml and 1 mg : 33 ml.

To remove all the big particles which create cracks and defects on thin film, a series of processes were applied to the solution. First of all, the solution is stirred at 1200 rpm for 1 hour at magnetic stirrer. After stirring, the solution was put in to ultrasonic bath for 45 minutes – 60 minutes to solve the big particles in the solution. Another ultrasonic application which is ultrasonic homogenization was also used to remove the small particles. Ultrasonic homogenizer generates high power ultrasonic pulsed waves which can disperse the particles in the solution. Figure 2.8 shows the ultrasonic homogenizer device which located at Materials Chemistry Laboratory of Metallurgical and Materials Engineering Department.

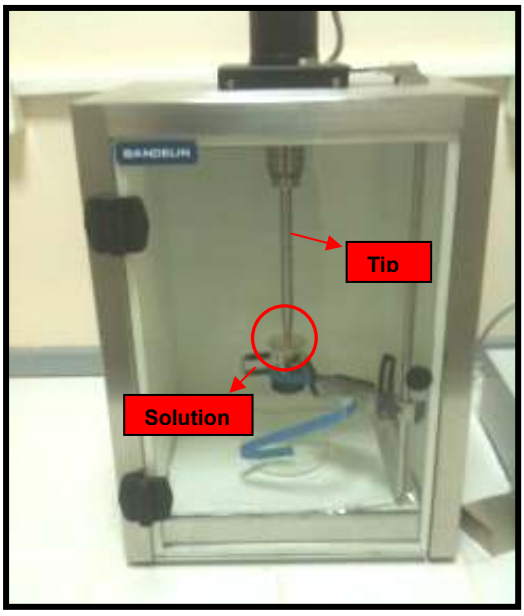

Figure 2.8 – The tip of the homogenizer was inside the solution. It sends pulsed ultrasonic waves.

After ultrasonic homogenization treatment, the solution was filtered with 3 micron filter to remove all the unsolved particles were removed from the solution before obtaining the final coating solution. Figure 2.9 shows the flow chart of the experimental path to the final solution.

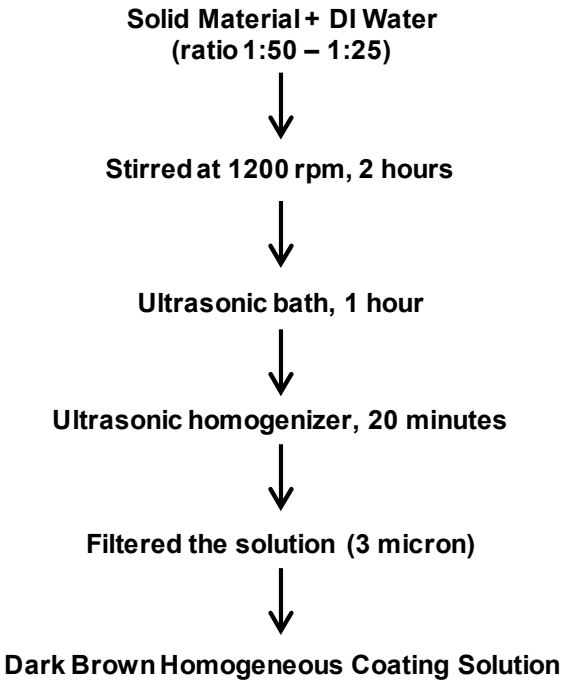

Figure 2.9 – Preparation flow chart of the final coating solution. Solid material and DI water mixed and stirred. After ultrasonic processes flittering is applied to obtain the dark brown homogeneous coating solution.

The final coating solution which is shown in Figure 2.10 has dark brown color and considerable viscosity. There is not any undissolved particles which can create cracks and undesired defects on the thin film.

Figure 2.10 – Dark brown coating solution, considerably viscous and ready for spin coating.

Viscosities of the coating solutions which were successful on coating were measured by Brookfield DV-E Viscometer located at Materials Chemistry Laboratory of Metallurgical and Materials Engineering Department. The device is shown in the Figure 2.11.

Figure 2.11 – Brookfield DV-E Viscometer was used to measure the viscosity of the final coating solutions.

As it is mentioned above, there is another way which is leaving the flocculated solution in rest in ambient conditions, to achieve a coating solution. The solution is turned to a dark brown sol with a considerable viscosity. This viscous solution was stirred and ultrasonically homogenized/dispersed to obtain homogenous solution without any particles. However, as it was explained before, the reaction of decomposition of hydrogen peroxide is not controllable so the final product was differs at each time.

2.2.2. Thin Film Coating Procedure

After the preparation of the coating solution, the solution was applied on to the substrates. It is essential to apply a cleaning procedure to substrates and tune the coating process to obtain crackles and uniform coatings. The cleaning procedure and the spin coating process will be explained in the following sub-sections.

2.2.2.1. Preparation of the Substrates

Si and SiN_x substrates were used in this study. Surface properties of thin films directly affect the electronic features of the film. If the surface is smooth and crack free, better results can be achieved. The substrates should be cleaned to obtain such crack free thin film results.

The substrates were cut in to desired shapes, mostly 2 x 2 cm, from 4 inch or from 6 inch substrates. Two steps of cleaning were applied to the substrates to get the substrates be ready before the spin coating process.

Figure 2.12 –Two step cleaning applied to 2 x 2 cm Si wafer before spin coating process.

Most of the silicon wafer surfaces show hydrophobic behavior, possibly due to some organic contaminations. So the liquids partly wet the surface of the substrate or they could not even wet the surface of the substrate after spin coating. All the dropped solution was bounced-off from the surface after spinning. Base/acid cleaning was applied to remove any residue creating hydrophobic behavior.

The wafers were kept in 1 wt % sodium hydroxide (NaOH) solution in ultrasonic bath for 15 minutes. After base cleaning, they put into 2 wt % hydrochloric acid (HCl) for 15 minutes in ultrasonic bath. The wafers were rinsed with DI water after acid cleaning and dried at 100 °C for 10 minutes before the second step of cleaning. The flow diagram of the two-step base/acid cleaning is given in Figure 2.13.

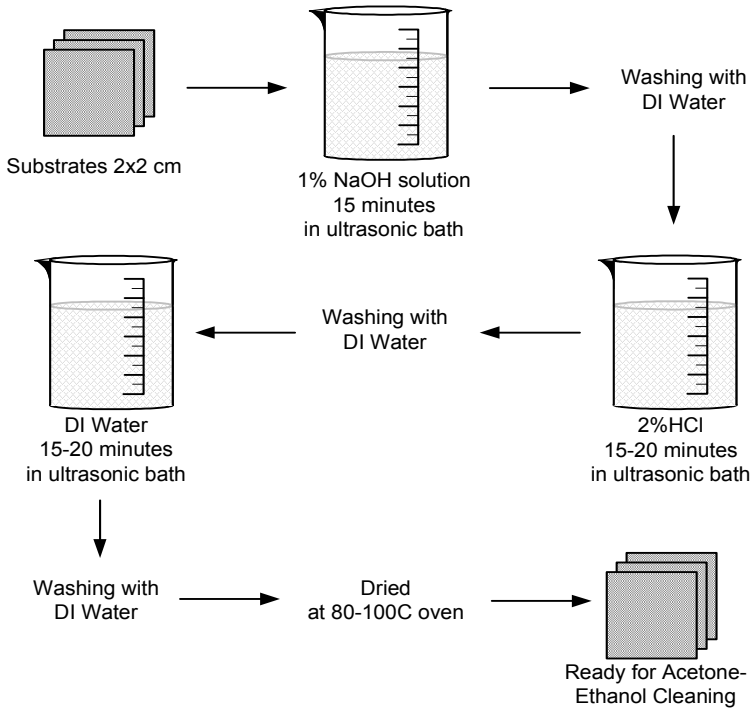

Figure 2.13 – Flow diagram of the base/acid cleaning, substrates cleaned in base and acid and then rinsed with water. They were dried in an oven to be ready for the second step cleaning.

Base/acid cleaning was applied only to the substrates show hydrophobic features. Most of the SiN_x substrates do not show such hydrophobic behavior. Possibly the nitride molecules do not allow to stick the molecules which causes hydrophobia, on top of the substrate.

Figure 2.14 – Two square wafers are in the ultrasonic bath while in the cleaning process.

Both Si and SiN_x substrates were cleaned with acetone, ethanol and rinsed with DI water to remove all particles and the contamination from the surface before the spin coating process.

First of all, the substrates are washed with DI water and kept in the acetone in ultrasonic bath for 15 minutes – 20 minutes. After this step, they were washed with ethanol and put into ethanol in ultrasonic bath for 15 minutes – 20 minutes.

Finally, the substrates were washed with DI water and DI water put into DI water in ultrasonic bath for 15 minutes – 20 minutes. After the entire ultrasonic bath processes the substrates were dried in the 80 °C – 100 °C oven for 10 minutes. The flow diagram of the acetone ethanol cleaning is given in Figure 2.15.

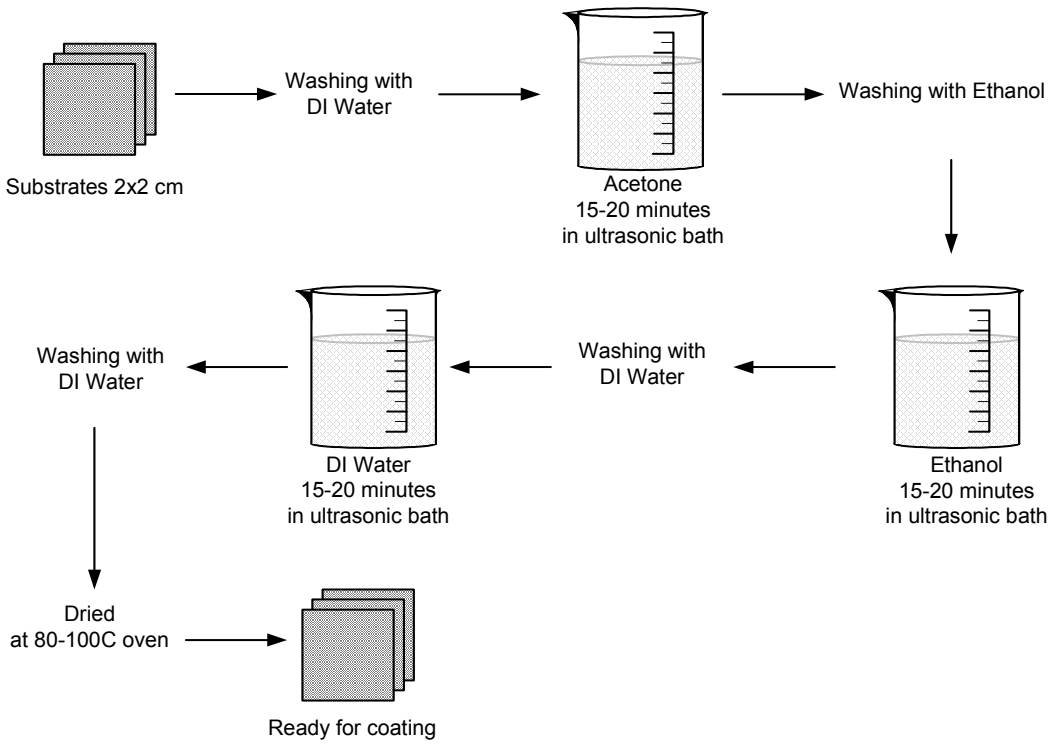

Figure 2.15 – Acetone, ethanol, DI water cleaning flow. The substrates were ultrasonically cleaned with acetone and ethanol and then rinsed with DI water. They were dried in an oven to be ready for spin coating process.

2.2.2.2. Spin Coating

As it is mentioned in section 1.5.2, thin films of sol-gel solutions can be deposited by spin coating, dip coating, and spray process techniques. Possibility of film thickness adjustment, clean process, and homogenous distribution of the film features makes the spin coating technique the most preferred one for single side thin film coatings processes [25, 41, 42].

Figure 2.16 – Programmable spin coater was used for thin film coating process.

Spin coating process was performed by using a spin coater (Laurell WS-400B-GNPP/LITE) which is shown in Figure 2.16. After solution preparation and the substrate cleaning, spin coating was performed onto Si and SiN_x substrates. Enough amount of solution was put onto the substrate by using transfer pipettes. Figure 2.17 shows the amount of the sol on to the substrate just before the spinning starts.

The thin film thickness and the quality can be adjusted by changing the spin rate of the spin coater. In this study, films were coated with one step and two step spin coating processes. The spin coater can be programmed to different acceleration and speed settings.

In one step spin coating applications, the spin coater starts to spin with programmed acceleration till the spinning speed reaches to the desired rate. Spinning was stopped after the programmed time period. Various spin rates 1000 rpm to 4000 rpm were applied for one step spin coating processes.

Figure 2.17 – Before spin coating, enough amount of solution was put on to the surface of wafer to cover it.

In two step spin coating applications, first slower step was used to spread the solution homogenously on the surface of the substrate. First step does not go on more than ten seconds. The second step follows the first step without stopping. The second step is like the one step spin coating process. The spin coater starts to spin with programmed acceleration till the spinning speed reaches to the desired rate. Spinning was stopped after the programmed time period. Best coatings were obtained with two step applications.

The spin coated sample is ready for the annealing step which reduces the oxygen state of the vanadium pentoxide to lower levels.

Thicknesses of the thin films which were coated at different spin rates were measured by “Veeco Dektak 8 Surface Profiler” located at METU-MEMS Center. Figure 2.18 shows the Veeco Dektak 8 Surface Profiler.

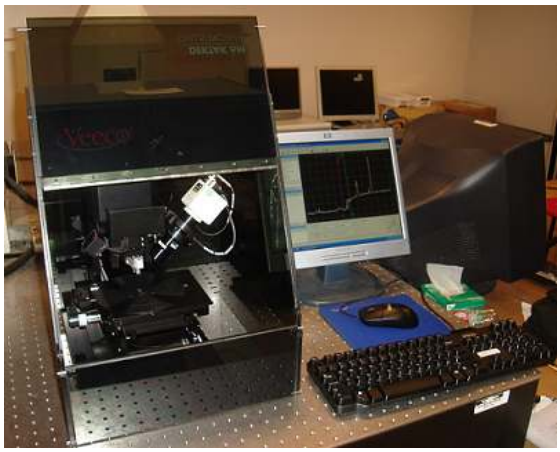

Figure 2.18 – Veeco Dektak 8 Surface Profiler is used for thickness measurement of the spin coated thin films.

In the following section solution preparation and thin film coating results will be presented.

2.3. Solution Preparation and Thin Film Coating Results

The explained solution preparation and thin film coating procedures were applied to obtain high quality vanadium oxide thin films on Si and SiN_x substrates.

2.3.1. Solution

VO_x coating solution preparation steps are summarized basically in Figure 2.19.

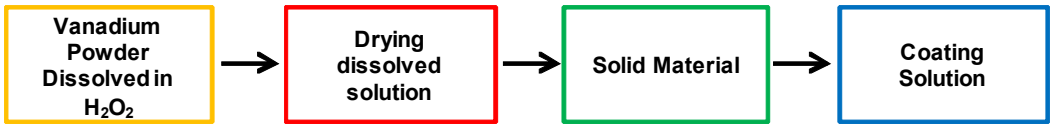

Figure 2.19 – Major solution preparation steps, vanadium powder dissolved in hydrogen peroxide, the solution was dried to obtain solid material and the solid material solved in DI water for final coating solution.

2.3.1.1. Solid Material Preparation Trials

The ratio of the vanadium powder and hydrogen peroxide is very important to achieve the desired coating solution. If the ratio is low, the dried solution gives very little solid material product. On the other hand, if the ratio is higher than an appropriate ratio, unsolved vanadium powders were remains in the solution after the reaction. To obtain the best mixing ratio trials given in the Table 2.1 were done.

The best results were achieved with the ratio of 1 g : 100 ml vanadium powder to hydrogen peroxide. The solution that was obtained by the dissolution of the vanadium in the hydrogen peroxide was dried at 80 °C for 24 hours and solid material was formed.

Table 2.1 – Dissolving vanadium powder in hydrogen peroxide trials and mixing ratios. Every dissolving trial has a color code (light grey, dark grey and grey). Light Grey: less dense solutions, Dark Grey: vanadium powder was remains, Grey: desired solution.

Trial Number	Vanadium Powder (mg)	H_2O_2 (ml)	Ratio (mg/ml)
1	200	100	2.00
2	200	50	4.00
3	100	20	5.00
4	100	5	20.00
5	100	10	10.00
6	250	25	10.00
7	250	25	10.00
8	250	25	10.00
9	250	25	10.00
10	250	25	10.00
11	250	25	10.00
12	250	25	10.00
13	250	25	10.00
14	250	25	10.00
15	400	40	10.00
16	400	40	10.00

Figure 2.20 shows the XRD pattern of the powdered solid material was mostly match with $V_2O_5 \cdot nH_2O$ structure. $V_2O_5 \cdot nH_2O$ peaks are on the major peaks of the sample.

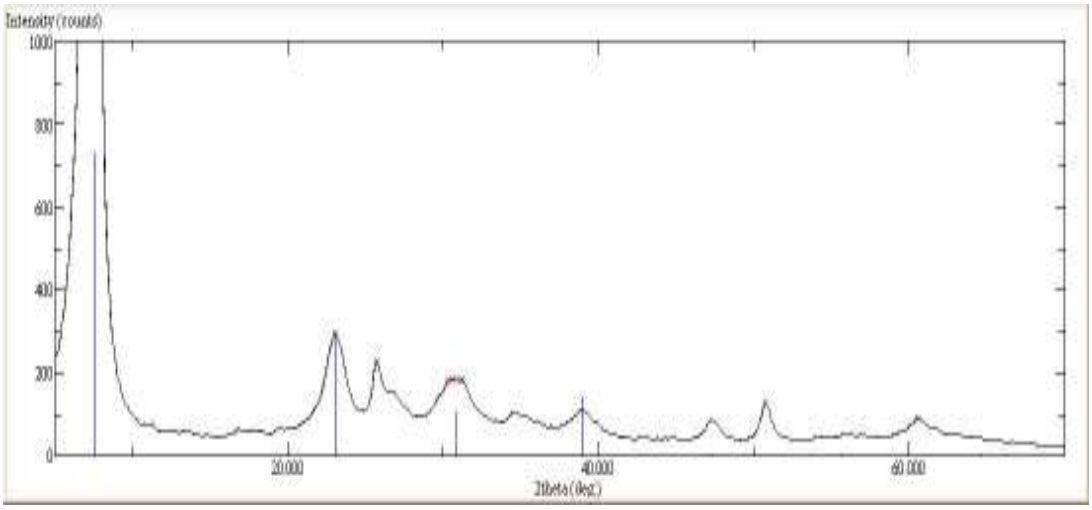

Figure 2.20 – XRD pattern of solid material (blue peaks are $V_2O_5 \cdot 1.6H_2O$), The major peaks are at (2θ = 8°, 22°, 31° and 39°).

TGA was done in air and nitrogen environments between 25 °C and 550 °C to see the mass change of the solid material in respect to temperature. Following TGA result is taken from the sample which is not annealed ($V_2O_5 \cdot 1.6H_2O$). The major weight loss is happened at lower temperatures and the reduced mass is more than 10% of the total mass. At the final, total weight loss is around 15 % of the beginning weight. Figure 2.21 shows the TGA results of the not annealed sample in N_2 environment between 25 °C and 550 °C. This result is an evidence of the loss of H_2O from the $V_2O_5 \cdot 1.6H_2O$ structure. In the light of TGA, the samples annealed at temperatures higher than 350 °C will loss the entire hydrogen dioxide from its structure.

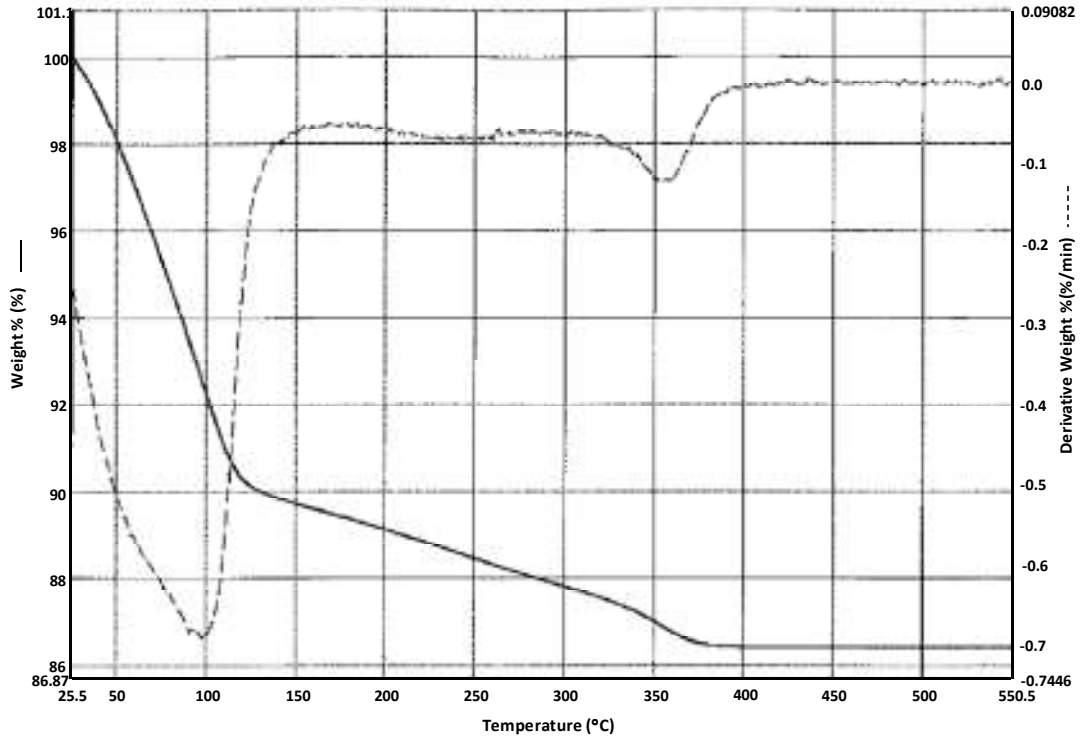

Figure 2.21 – The TGA curve of not annealed sample in N_2 environment between 25 °C and 550 °C.

The powdered solid material was annealed under air conditions at 370 °C for 2 hours. The color of the solid material was dark brown before the annealing process and light dark after the annealing process. The XRD pattern of the annealed sample proves the TGA of the sample. The entire hydrogen dioxide was removed and V_2O_5 crystal structure (JCPDS 41-1426) formed after the annealing. Figure 2.22 shows the XRD pattern of the solid material powder annealed at 370 °C for 2 hours.

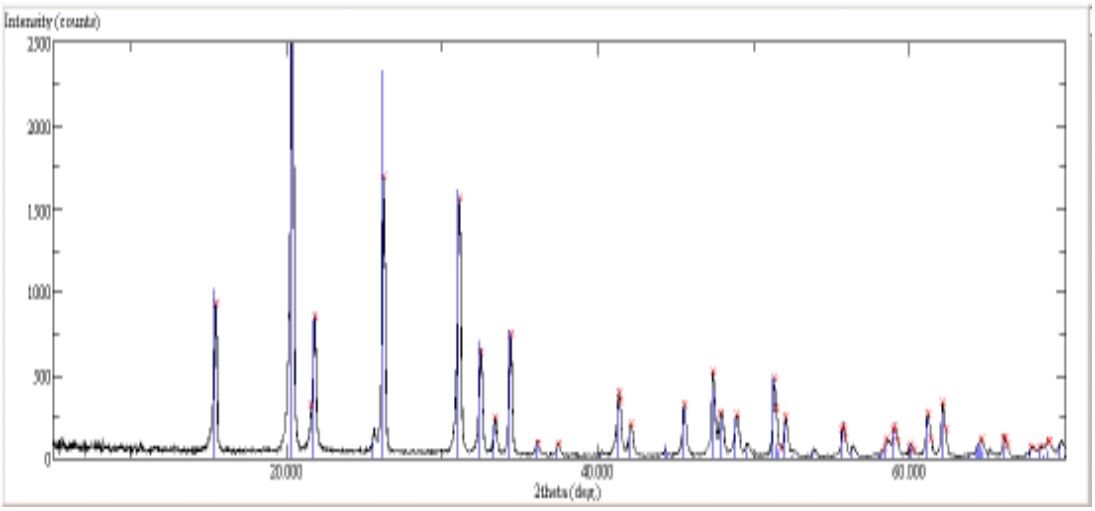

Figure 2.22 – XRD Pattern of solid material powder annealed at 370 °C for 2 hours (blue peaks are V_2O_5) JCPDS card no: 41-1426.

One of the possible V_2O_5 to VO_x reducing annealing environments is nitrogen. To see the effect of the nitrogen environment on solid samples, powdered and annealed samples was given to TGA analysis. TGA analysis result of the sample (annealed at 370 °C for 2 hours) which analyzed from 25 °C to 500 °C in nitrogen was given in Figure 2.23. It is expected that the weight reduction occurs between 300 °C and 450°C. As it can be seen from the figure, the results are consistent with the expectations. However, the weight reduction was not as much as expected, it was around four in a thousand.

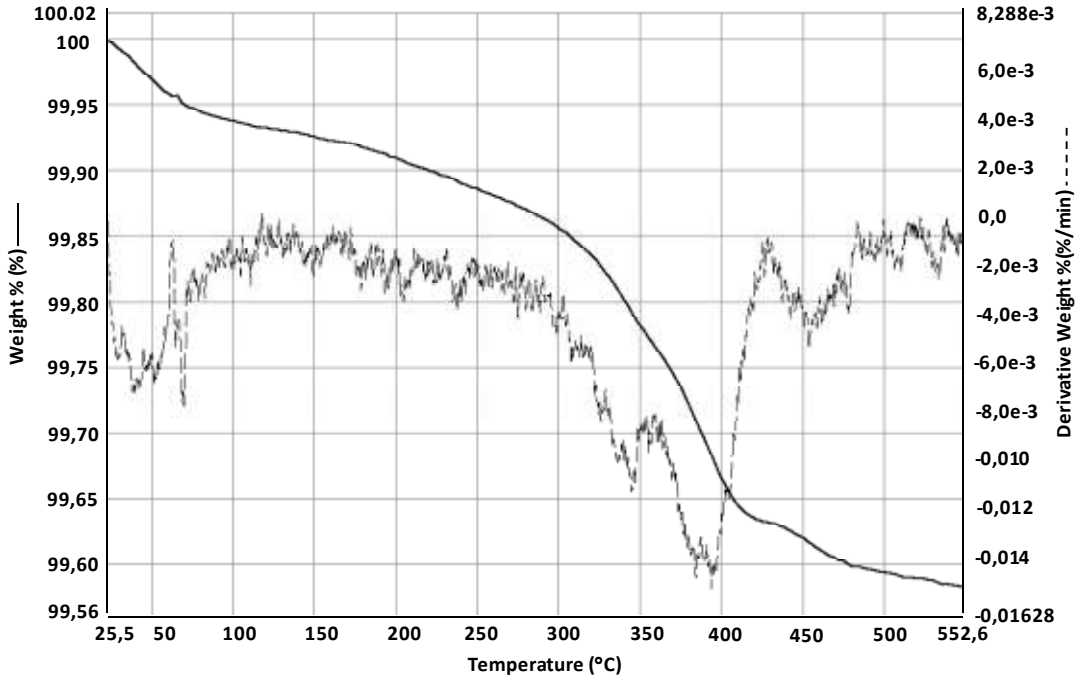

Figure 2.23 – The TGA curve of V2O5 sample in N2 environment between 25 °C and 550 °C.

Weight loss in the interval of 300 °C – 400 °C possibly means that the sample losing O_2 at that temperature interval. V_2O_5 to VO_x reduction can be happened at around these temperatures in nitrogen. As it is mentioned, the ratio of the lost weight was not as much as expected. To be sure the results, the films should be annealed under nitrogen environment at the temperatures around 350 °C – 400 °C and the XRD results of annealed films should be evaluated. The annealing temperature, annealing duration, and the nitrogen purification can change the results of the annealing process.

2.3.1.2. Coating Solution Preparation Trials

After analyzing the solid material, the coating solution was prepared by adding some amount of DI-water into solid material. The following table shows the solution

preparation trials (Table 2.2). Adhesion of the solution was changed due to the ratio of solid material and DI-water.

Table 2.2 – Coating solution preparation trials with solid material and DI water. The trials are colored in respect to the successfulness of the trials. Light grey colored trials have lower densities, grey colored trials are successful enough for spin coating and dark grey colored trials are denser and have lots of unsolved solid particles.

Sample #	V-Powder + H_2O_2	80 °C Drying Solid Material	370 °C Annealed V_2O_5 Powder	V_2O_5 + H_2O	Solid Material + DI Water
1	X	X	-	-	(0.1/10) 1:100
2	X	X	-	-	(0.15/10) 1:66.7
3	X	X	X	X	Flocculated
4	X	X	-	-	(0.2/10) 1:50
4.1	X	X	-	-	(0.3/10, 1:33)
5	X	X	-	-	(0.4/10, 1:25)
5.1	X	X	-	-	(0.33/10, 1:30)
5.2	X	X	-	-	(0.33/10, 1:30)
6.1	X	X	-	-	(0.33/10, 1:30)
6.2	X	X	-	-	(0.3/10, 1:33)
7.1	X	X	-	-	(0.3/10, 1:33)
8.1	X	-	-	-	Flocculated
9	X	X	-	-	(0.3/10, 1:33)
10	X	X	-	-	(0.3/10, 1:33)

Best coating results were achieved with the ratios between 1 mg : 30 ml to 1 mg : 33 ml. Viscosities of the successfully coated solutions were measured. Table 2.3 shows the viscosities of the coating solutions.

Table 2.3 – Measured viscosities of the coating solutions

Solution #	cP
6.2	5.78
7.1	5.8
8.1	5.8
9	5.75
10	5.77

The solutions were passed all the solution preparation steps which are explained in detail in Section 2.2. The coating trials were done with the solutions were prepared at ratios between 1 : 30 – 1 : 33 of solid material and DI-water and had viscosity between 5.75 and 5.80.

2.3.2. Spin Coating

Spin coating process was applied on to the cleaned Si and SiN_x substrates. Best results were achieved with SiN_x substrates. Solutions can easily stick to the SiN_x substrates. However, some uncoated areas can be observed while the Si substrates were used for coating thin films due to the hydrophobic behavior of the surface.

(a) (b)

Figure 2.24 – (a) Not coated, clean SiN_x substrate, (b) totally coated substrate.

About two hundred trials were done till the appropriate spin coating steps and the spin rates of the process. The following table shows some of the spin coating trials with different solutions. Two step spin coatings gave the best results. First step of the

coating has lower spin rate around 400 rpm – 500 rpm and takes about 5 seconds. The aim of the first step is cover all the surface of the wafer and spread the solution equally. Second step has higher spin rate about 2000 rpm and takes about 60 seconds to 75 seconds.

Table 2.4 – Spin coating trials

#	Sample	Spinning Rate (rpm)	Acc.	Duration
1	1_A	2000	005	1 min
2	1_B	1000	005	1 min
3	1_C	1000	005	1 min
6	2_B	750	005	1 min
7	2_C	2000	005	1 min
8	3_A	2000	005	1 min
9	4_A	1500	005	1 min
11	4_C	3000	005	1 min
26	5.2_C	1000/3000	003/005	15 sec / 40 sec
27	5.2_D	3000	0.05	1 min
39	6.1_A	3000	$7.14r/s^2$	1 min
44	6.1_F	2500	$7.14r/s^2$	40 sec
47	6.1_I	350/3000	001/005	10 sec / 1 min
48	6.1_J	100/500/3000	001/001/005	5 sec / 5 sec / 45 sec
49	6.1_K	100/200/500/2000	001/001/001/005	5sec/5sec/5sec/45sec
50	6.1_L	4000	25	1 min
51	6.1_M	4000	35	1 min
54	6.1_P	500/2500	001/005	5 sec / 45 sec
62	7.1_E	450/2000	001/005	5 sec / 45 sec
63	7.1_F	450/1750	001/005	5 sec / 45 sec
64	7.1_G	450/2000	001/005	5 sec / 45 sec
74	8.B	4000	25	1 minute
75	8.C	3000	15	90 seconds
76	8.D	450/2000	001/005	5 sec / 45 sec
77	8.E	450/2000	001/005	5 sec / 45 sec
84	9_f	450/2000	001/005	5 sec / 1 min
99	10_d	450/2000	001/005	5 sec / 75 sec

Thicknesses of the successfully coated wafers were measured. The relation between the spin speed and the thickness is consistent. The thickness of the thin film gets lower with high spin speeds (Table 2.5).

Table 2.5 – Spin speed and thickness relation of the thin films

Spin speed (rpm)	Thickness (nm)
1000	57
2000	33.5
3000	21

The thin films are ready for annealing step. The reduction process will be done by annealing in different environment. The annealing process and the results will be presented in the following chapter.

CHAPTER 3

ANNEALING OF VO_x THIN FILMS

Annealing is used to create crystal structures or increase/decrease the oxygen states of the metal oxide thin films. Different annealing environments such as air, vacuum, nitrogen, hydrogen, CO, CO_2, and some other gas mixtures used as reducing annealing atmospheres. [25, 28, 31, 32, 41, 44]. Annealing atmosphere, temperature and duration are the critical parameters for annealing process. It is possible to change the result of the process by changing these critical parameters.

This chapter presents the annealing procedure and the characterization of the VO_x thin films. Section 3.1 gives information about the annealing trials of vanadium oxide thin films in the literature. Section 3.2 describes the annealing procedures to reduce the oxygen state of the VO_x and Section 3.3 summarizes the results of the annealing process.

3.1. Annealing Trials of VO_x Films in the Literature

It is possible to reduce the oxygen state of VO_x with annealing atmospheres such as air, vacuum, nitrogen, hydrogen, CO, CO_2, and some other gas mixtures; however, as it was mentioned annealing temperature and the duration of the annealing are the other critical parameters for reduction process. There are many possible stochiometries and structures of vanadium oxide such as VO, V_2O_3, VO_2, V_3O_7, V_4O_9, V_6O_{13}, V_2O_5 [31, 45, 46].

The following table shows the results of VO_x annealing under different environments, durations, and pressures (Table 3.1). When the literature was surveyed many teams used various annealing processes to reduce the oxygen state of the VO_x.

Takahashi and colleagues used following annealing process for reduction of V_2O_5. Two step annealing was used to reduce sol-gel derived V_2O_5 thin film to lower VO_x states. First of all, the film was annealed at 400 °C in hydrogen ambient for 2 hours and then annealed at 500 °C in nitrogen ambient for 1 hour. It is stated in the paper that if the annealing times were shortened mixed VO_x states such as V_3O_7 and V_6O_{13} observed on the thin film [25, 47].

Table 3.1 – Annealing conditions to reduce V_2O_5 to lower oxygen states.

Temperature	**Duration**	**Pressure**	**Gas Mixture**	
550 °C	2 hours	Low pressure	50 % CO – 50 % CO_2 [48]	$V_2O_5 \rightarrow VO_2$
500 °C 550 °C	2 hours 12 hours	-	H_2 / Ar 5 % [49]	$V_2O_5 \rightarrow VO_2$
500 °C – 550 °C	-	Appropriate pressure	CO / CO_2 [3, 31]	
400 °C – 500 °C	1-2 hours	Appropriate pressure	1st step H_2 [47] 2nd step N_2	
400 °C – 500 °C	20 -60 minutes	1 Pa – 2 Pa	Air [41, 43]	
1st 150-300°C 2nd 300-550°C	2 hours 2 – 90 hours	Appropriate pressure 0.8 Pa – 5 Pa	Air or Water Vapor H_2 or Air	
300 °C 500 °C	1hour 2hours	Appropriate pressure	N_2 [27]	
550 °C 600 °C	30min 5min	-	N_2 [50]	$V_2O_5 \rightarrow VO_2$
400 °C – 500 °C	2 hours	6 Pa - 7 Pa	Air [51, 52]	$V_2O_5 \rightarrow VO_2$

Ugaji and Hibino reported that at 100 °C treated $V_2O_5 \cdot nH_2O$ turned to 2D-V_2O_5 (1 hour), Heating more than 305 °C [47], 290 °C [36] the sample turned to orthorhombic V_2O_5 (air).

Other trials can be seen in literature such as V_2O_5 thin films were annealed in vacuum heating under 1 Pa – 2 Pa, 480 °C for 20 minutes [26, 41, 43]. The key point is the reduction steps of V_2O_5 thin film. The V_2O_5 structure does not directly reduce the VO_2 structure. When the annealing temperature is high enough the oxygen escape from crystal structure and V_3O_7 phase appears. Different phases also appear with different annealing temperature and times. The process of $V_2O_5 \rightarrow V_3O_7 \rightarrow V_4O_9 \rightarrow V_6O_{13} \rightarrow VO_2$, namely from V_nO_{2n+1} (n = 2, 3, 4, 6) to VO_2. The recent researches indicate that V_3O_7, V_4O_9, V_6O_{13} could exist as one phase in film due to the different heating condition, the type and intensity of intermediate phase of V_nO_{2n+1} (n = 2, 3, 4, 6) were different [26, 41, 43].

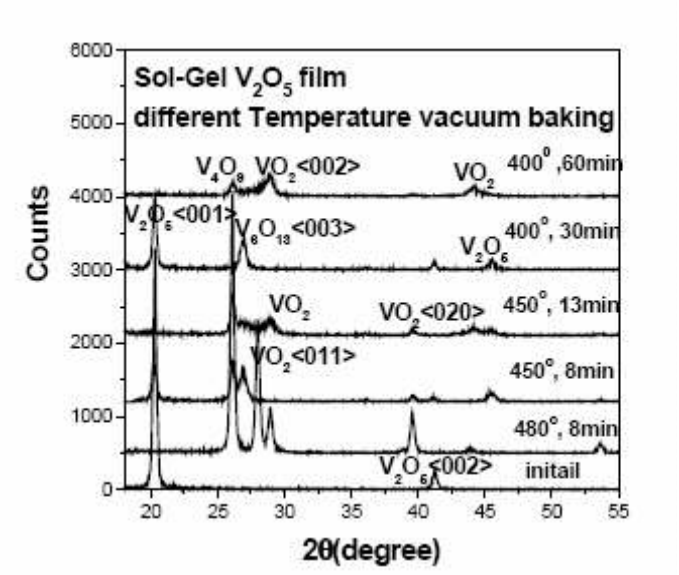

Figure 3.1 – XRD spectra of VO_x film reduced from vacuum heating of V_2O_5 film [41].

Many intermediate oxides exist between V_2O_5 to VO_2 [45]. These steps are represented below.

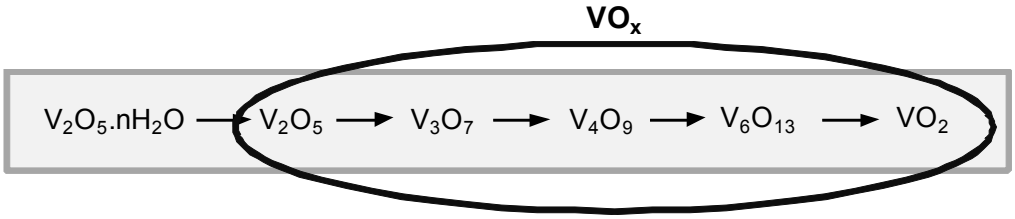

Figure 3.2 – V_2O_5 to VO_2 reduction steps.

Dachuan reported following annealing conditions. The V_2O_5 thin film was annealed in air at 150 °C – 300 °C for 2 hours and then heated in vacuum furnace at 300 °C - 550 °C for 2 hours – 90 hours. The pressure of the annealing furnace was 0.8 Pa – 5 Pa and the vacuum chamber was fed with low pressure H_2 or low pressure air. They can able to reduce the V_2O_5 thin film structure to VO_2 [42].

Takahashi and colleagues reported that they achieve V_2O_5 films when the samples annealed in air. If the annealing temperature is less than 350 °C the films were amorphous. When the annealing temperature was increased around 400 °C, the films were became crystallized V_2O_5. They also tried to anneal some samples in N_2 environment. They achieve crystallized films which were annealed around 400 °C - 500 °C for 2 hours in N_2. However the results were not consistent with known vanadium oxides. They stated that the films were composed of at least two different substances [27].

As it is mentioned, there are many different reducing annealing ways to obtain VO_x states. The appropriate annealing process can be found considering the limitation of own experimental processes. The annealing procedure of this study will be presented in the following section.

3.2. Annealing Procedure

In this study, main reason behind the annealing is reducing the V_2O_5 thin film structure to the lower oxygen states of VO_x. To achieve this objective many annealing environments, different temperatures and various annealing periods were applied to the thin films (Table 3.2).

Table 3.2 – Various annealing trials were tried to find the appropriate annealing procedure.

#	Drying	Air 370 °C	Air 400 °C	N_2 200 °C	N_2 370 °C	N_2 400 °C	Vacuum (~E-5 Torr) 400 °C (RTA)	5% H_2/N_2 400 °C (RTA)	5% H_2/N_2 420 °C (RTA)	25% H_2/N_2 400 °C (RTA)	10% H_2/N_2 420 °C (RTA)	10% H_2/N_2 410 °C (RTA)	20% H_2/N_2 410 °C (RTA)	30% H_2/N_2 410 °C (RTA)	40% H_2/N_2 410 °C (RTA)
1	X														
2	X	2 h													
3	X	2 h			2 h										
4	X			2 h	2 h										
5	X		2 h												
6	X			2 h											
7	X	2 h				5 h									
8	X	2 h					2 h								
9	X	2 h								2 h					
10	X							20 min							
11	X							30 min							
12	X							45 min							
13	X								20 min						
14	X								30 min						
15	X					2 h (2nd)					2 h (1st)				
16	X					(2nd)						(1st)			
17	X					(2nd)							(1st)		
18	X					(2nd)								(1st)	
19	X					(2nd)									(1st)

Heat treatment of thin films begins with the drying step. Drying was done in an oven at 80 °C for 30 minutes to 1 hour or it was done in ambient conditions.

Dried films should be annealed after drying process to obtain the desirable VO_x structure. Dried film has amorphous structure which contains vanadium, oxygen and the hydrogen. Hydrogen dioxide molecules can be observed by XRD on the dried films. Annealing is removed the undesired hydrogen molecules and the change the structure of the film amorphous to polycrystal.

Annealing environment and the temperature is an important factor to obtain the final thin film structure. In this study annealing temperature was varied from 200 °C to 420 °C and the annealing environment was chosen as air, nitrogen, vacuum or hydrogen (5 % H_2/N_2 – 40 % H_2/N_2). Vacuum and hydrogen environment annealing were done with AnnealSYS RTA Tube furnace which placed at GÜNAM clean room. Figure 3.3 shows the RTA Tube Furnace.

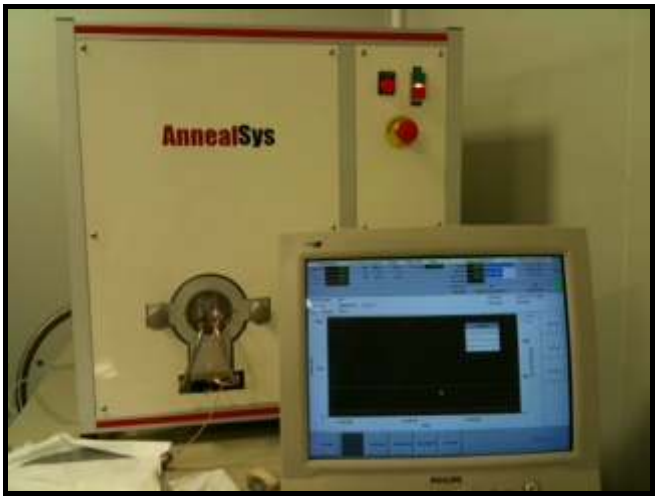

Figure 3.3 – RTA tube furnace which allows annealing under vacuum and hydrogen environments.

Nitrogen, vacuum, and hydrogen environments were used for reducing the VO_x to lower oxygen states. Reducing annealing atmosphere should be removed from the oxygen. In the literature hydrogen is the most used annealing environment for the low temperature process. Nitrogen and air environments were used to achieve to crystal/poly-crystal structures.

In vacuum or nitrogen environment the following reduction reaction is occurred:

$$V_2O_5 \rightarrow V_2O_4 + ½\ O_2 \tag{3.1}$$

In hydrogen environment the following reduction reaction is occurred:

$$V_2O_5(s)+(5-X)H_2(g)\rightarrow V_2O_x(s)+(H_2O)_{5-X}(g) \quad (3.2)$$

One or two step annealing was applied on the samples. One step annealing was done to remove the undesired hydrogen molecules from the structure and mostly to achieve orthorhombic vanadium pentoxide (V_2O_5) structure. On the second step of annealing the major objective is to achieve lower oxygen states of the VO_x such as V_4O_9, V_6O_{13}, VO_2 or multi state VO_x structure. While the reducing annealing occurs, oxygen molecules apart from the VO_x structure the oxygen state lowers.

Furthermore, some of the samples were firstly annealed under reducing atmosphere (hydrogen) and then annealed under second annealing environment.

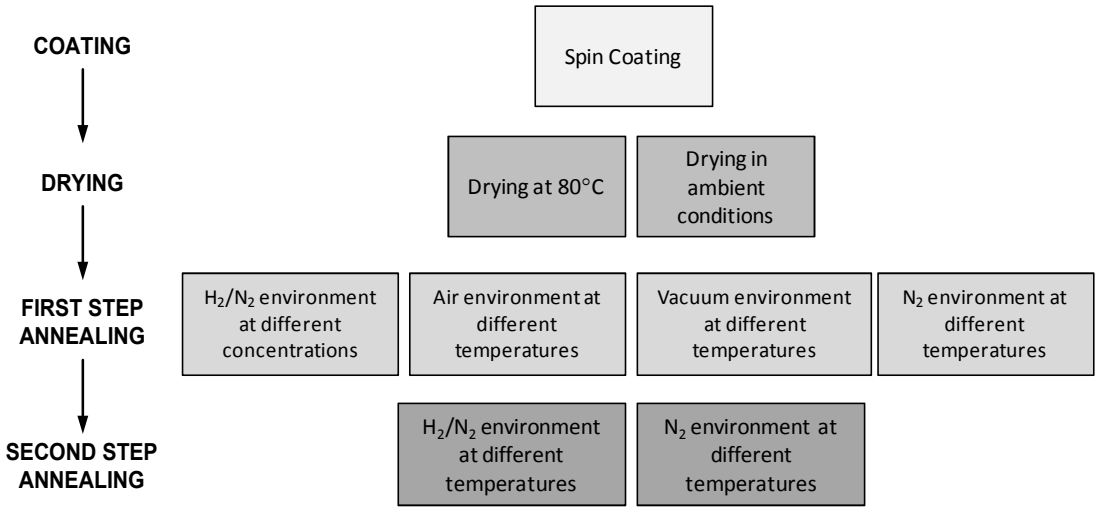

Figure 3.4 – Annealing flow chart; drying was applied after spin coating, two step annealing was used to reduction of V_2O_5 to VO_x.

Annealed samples were characterized by XRD. The structure of the final thin films was analyzed by XRD measurements. XRD analysis were performed between angles

of ($2\theta = 10° - 80°$) with Cu(Kα) radiation. The results of the annealing trials will be presented in the following section.

3.3. Annealing Results

Successfully coated films were annealed to obtain VO_x structured films. Table 3.3 shows the annealing trials and results of the XRDs of those trials.

Table 3.3 – Reducing V_2O_5 to VO_x annealing trials.

#	Drying	Air 370 °C	Air 400 °C	N_2 200 °C	N_2 370 °C	N_2 400 °C	Vacuum (~E-5 Torr) 400 °C (RTA)	5 % H_2/N_2 400 °C (RTA)	5 % H_2/N_2 420 °C (RTA)	25 % H_2/N_2 400 °C (RTA)	10 % H_2/N_2 420 °C (RTA)	XRD Results
1	X											$V_2O_5 \cdot nH_2O$
2	X	2 h										V_2O_5
3	X	2 h			2 h							V_2O_5
4	X			2 h	2 h							V_2O_5
5	X		2 h									V_2O_5
6	X			2 h								V_2O_5
7	X	2 h				5 h						V_2O_5
8	X	2 h					2 h					?
9	X	2 h								2 h		?
10	X							20 min				V_2O_5
11	X							30 min				V_2O_5
12	X							45 min				V_2O_5
13	X								20 min			V_2O_5
14	X								30 min			V_2O_5
15	X					2 h (2nd)					2 h (1st)	VO_x

First trials were done under air conditions. Later on, various temperatures and durations of annealing in nitrogen were tried as reducing atmosphere. However, these trials did not give the desired VO_x structure. Figure 3.5, Figure 3.6, and Figure 3.7 show the XRD patterns of the samples annealed in air and nitrogen environments. After all trials on air and nitrogen environments, vacuum and

hydrogen environments were used as reducing atmosphere. The results of the annealing under hydrogen and vacuum were different from the previous results. However, the XRD pattern of these trials could not be analyzed meaningfully. Various durations of hydrogen annealing were tried at different temperatures to find the appropriate reducing annealing atmosphere. Finally, one of the samples can be reduced to VO_x structure by two step annealing. The first step of the annealing was done under 10 % H_2/N_2 atmosphere for 2 hours at 420 °C, the second step was done under nitrogen atmosphere for 2 hours at 400 °C. The difference between the last trial and all the previous trials trial is the reducing atmosphere annealing was done first and for appropriate period of time.

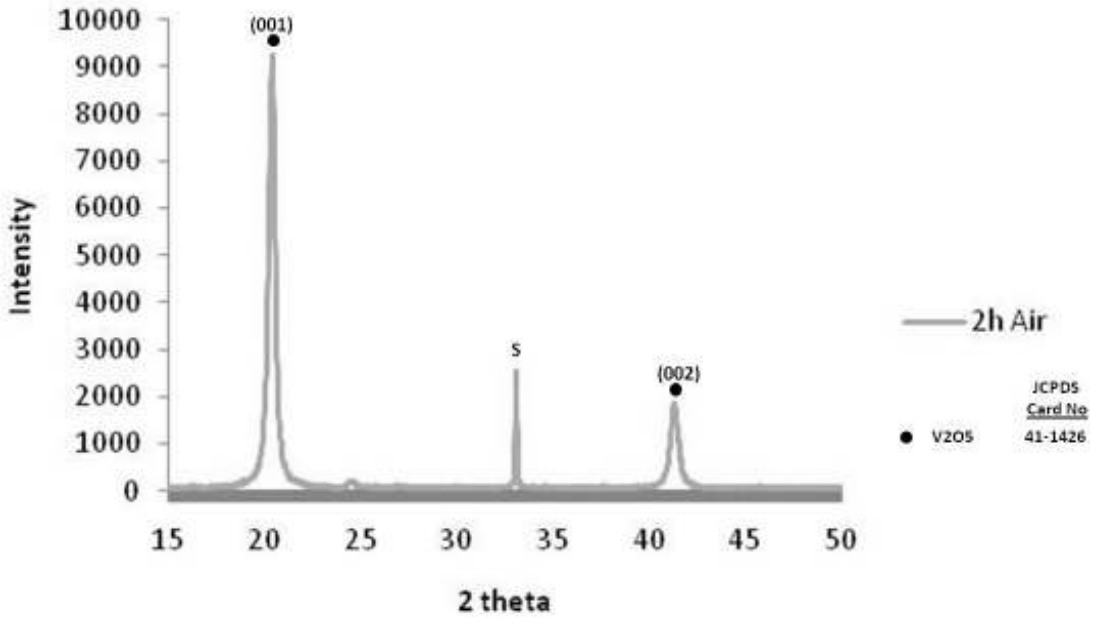

Figure 3.5 – The sample was annealed under air for 2 hours at 400 °C, there are two main peaks which are matched with (001) and (002) planes of V_2O_5 (JCPDS 41-1426), "S" peak comes from the substrate.

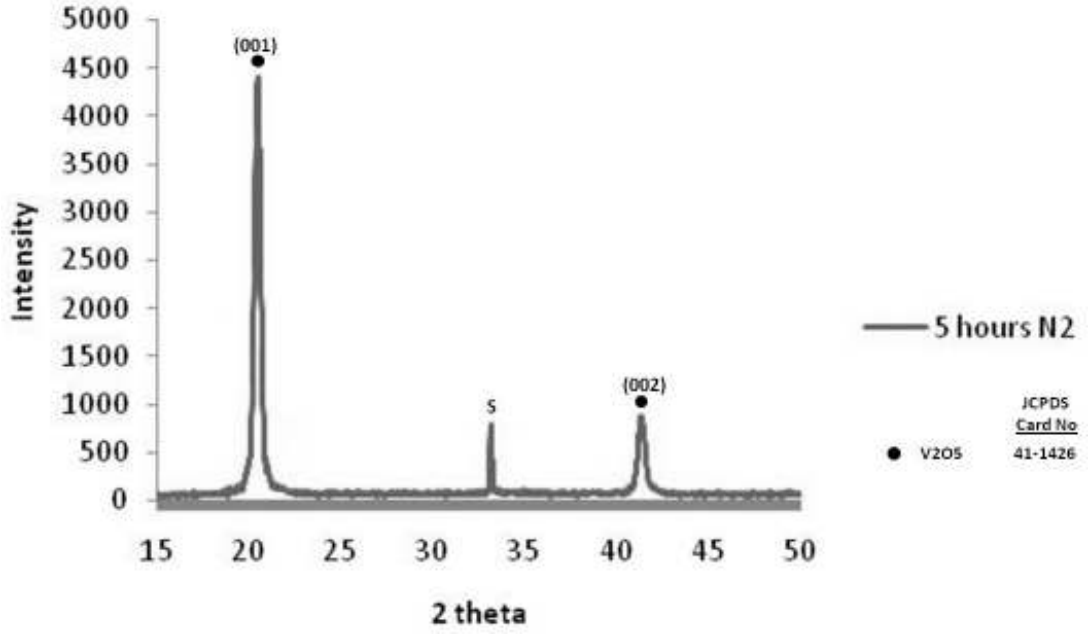

Figure 3.6 – The sample was annealed under nitrogen for 5 hours at 400 °C, there are two main peaks which are matched with (001) and (002) planes of V_2O_5 (JCPDS 41-1426), "S" peak comes from the substrate.

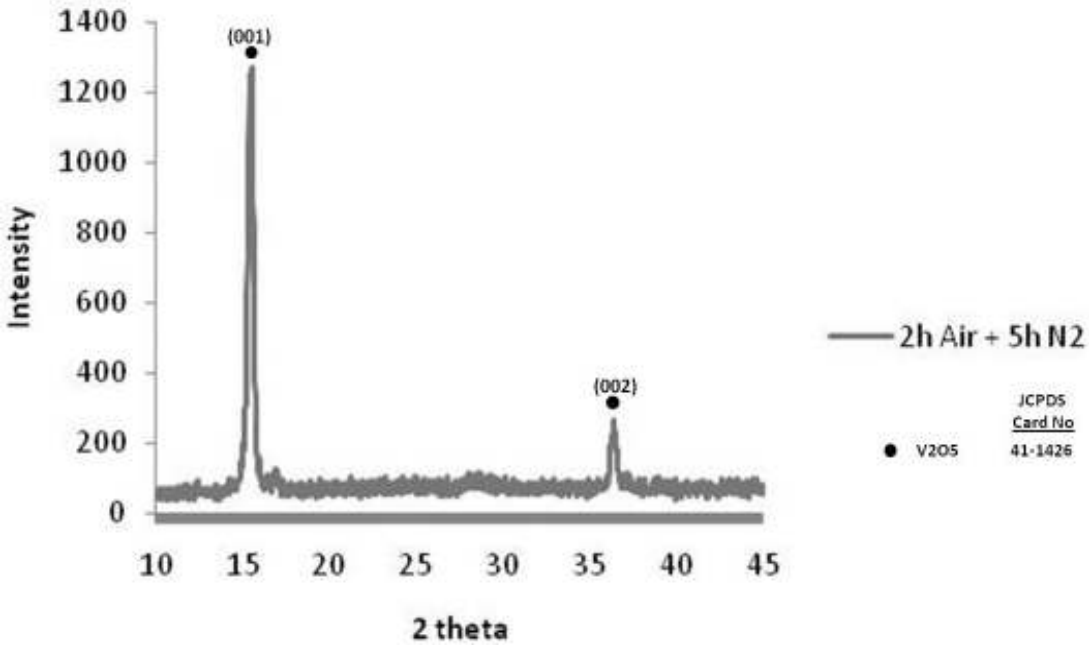

Figure 3.7 – The sample was annealed firstly under air for 2 hours at 400 °C and then under nitrogen for 5 hours at 400 °C, there are two main peaks which are matched with (001) and (002) planes of V_2O_5 (JCPDS 41-1426).

When the film is annealed under firstly hydrogen environment and then nitrogen environment, the reduction of V valances is happened. Figure 3.8 shows the XRD pattern of the sample which was annealed under firstly hydrogen environment and then nitrogen environment. The three major peaks are V_2O_5 (001), VO_2 (110), and V_2O_5 (002). The highest intensity peak is V_2O_5 (001). V_6O_{13} (002), and V_6O_{13} (110) peaks were also appeared in this sample.

All the next annealing trials were planned according to the successful two steps H_2 and N_2 annealing trial.

Table 3.4 presents the annealing plan for the reduction process of the samples.

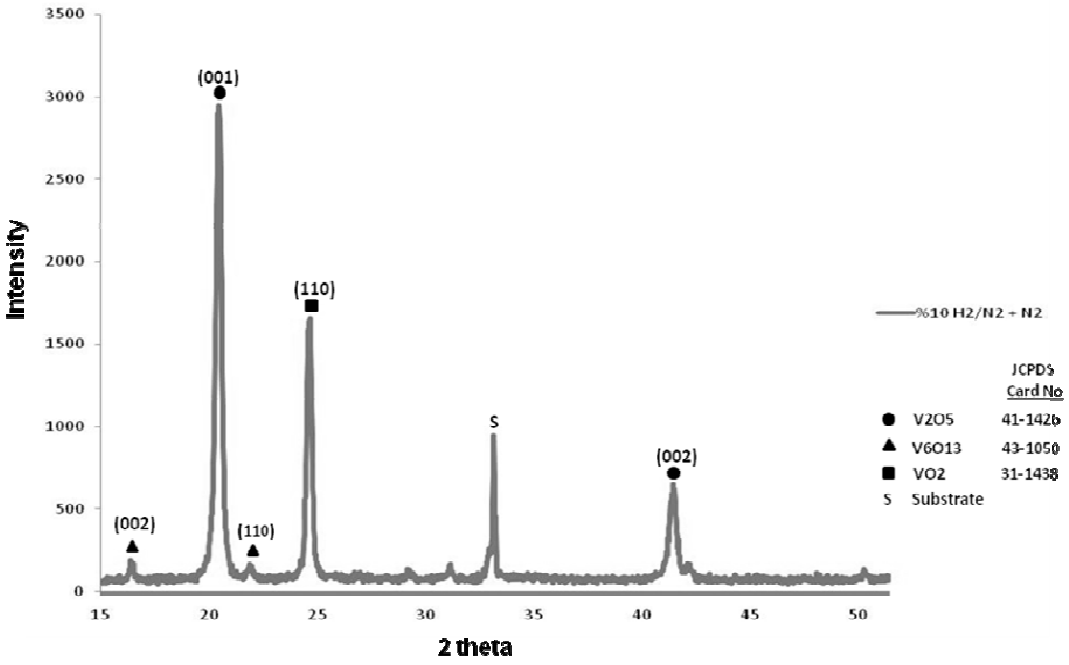

Figure 3.8 – The XRD pattern of the film annealed firstly under H_2/N_2 environment for 2 hours and then N_2 environment for 2 hours. V_2O_5, VO_2, and V_6O_{13} peaks are observed.

Table 3.4 – The annealing plan for the reduction process.

#	1st Annealing			2nd Annealing	
	Annealing Gas: H_2/N_2			Annealing Gas: N_2	
	Temperature	Gas Ratio	Annealing Period	Temperature	Annealing Period
1	410 °C	10 %	2 hours	410 °C	1 hour
2	410 °C	10 %	2.5 hours	410 °C	1 hour
3	410 °C	20 %	1.5 hours	410 °C	1 hour
4	410 °C	20 %	2 hours	410 °C	1 hour
5	410 °C	20 %	2.5 hours	410 °C	1 hour
6	410 °C	30 %	1.5 hours	410 °C	1 hour
7	410 °C	30 %	2 hours	410 °C	1 hour
8	410 °C	30 %	2.5 hours	410 °C	1 hour
9	410 °C	40 %	1 hour	410 °C	1 hour
10	410 °C	40 %	1.5 hours	410 °C	1 hour

The first annealing step is used for reducing the V_2O_5 to VO_x structure. The following reaction is occurred while the sample is under H_2 environment.

$$V_2O_5 + H_2 \rightarrow VO_x + H_2O \quad (3.3)$$

The annealing temperature set as 410 °C for all the steps, the ratio of hydrogen to nitrogen was changed in the interval of 10 % to 40 % and the annealing period was varied from 1 hour to 2.5 hours. The second step was kept fixed to 410°C in nitrogen atmosphere for 1 hour.

The results of these trials are presented in respect of the annealing period and reducing atmosphere concentration.

The reducing atmosphere was used as mixture of H_2 and N_2 gasses. As it is explained H_2 is used for reducing the V_2O_5 to lower VO_x states and inert N_2 is used to achieve O_2 free annealing atmosphere. The H_2 concentration of the annealing atmosphere determines the annealing period of the film. Higher H_2 concentration lowers the annealing period.

3.3.1. Annealing Time Dependency

XRD patterns of the films are given in following figures are indexed according to the standard powder patterns for polycrystalline, orthorhombic V_2O_5, tetragonal monoclinic V_6O_{13}, and VO_2 (JCPDS 41-1426, JCPDS 43-1050, and JCPDS 31-1438, respectively). Time dependency of the annealing is evaluated for different H_2/N_2 ratios of the annealing atmosphere. Figure 3.9 shows the XRD patterns of the samples which were annealed under the ratio of 10 % H_2/N_2 at 410 °C for different annealing durations.

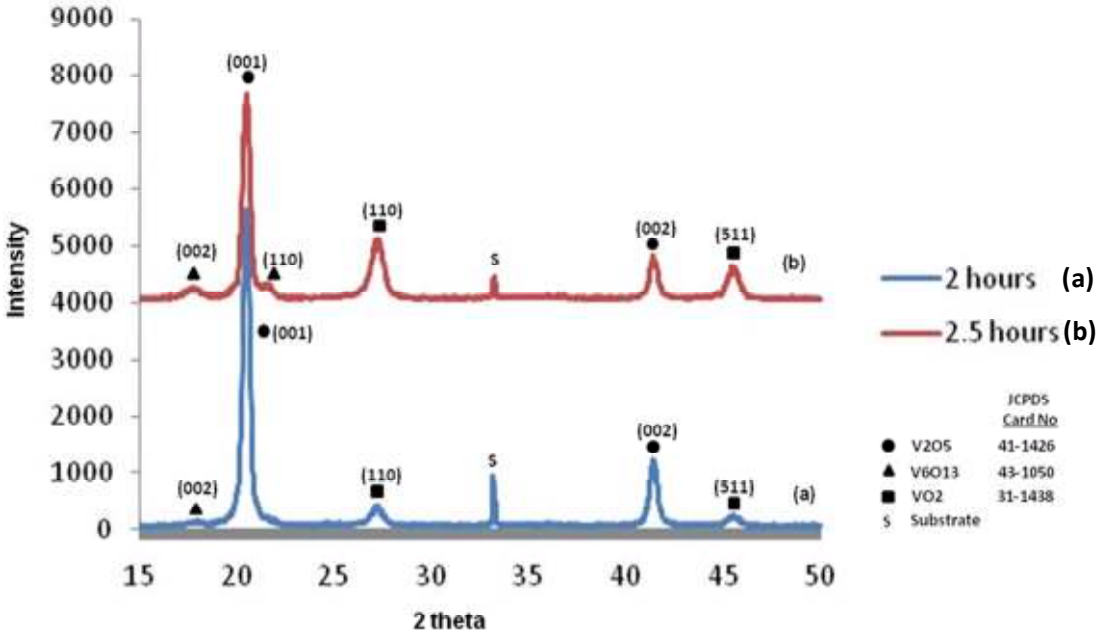

Figure 3.9 – XRD patterns of the films were annealed under 10 % H_2/N_2 environment at 410 °C for (a) 2 hours, (b) 2.5 hours and then both films were annealed in N_2 environment at 410 °C for 1 hour.

The major peaks are V_2O_5 (001) and V_2O_5 (002) for the sample is annealed for 2 hours. VO_2 (110), VO_2 (511), and V_6O_{13} (002) peaks has very low intensities. It is possible to say that the composition of the film is VO_x, however VO_x composition of the film is very close the V_2O_5 orthorhombic structure. Sample (b) was annealed

under 10 % H_2/N_2 atmosphere for more 30 minutes than the sample (a). As it is understood from the figure that the intensity of the V_2O_5 (001) and V_2O_5 (002) peaks are lower than the sample (a). VO_2 and V_6O_{13} peaks are become distinctive and another V_6O_{13} (110) peak is also appeared in the XRD pattern of the sample.

Figure 3.10 shows the annealing time dependency of the samples which were annealed under 20 % H_2/N_2 environment at 410 °C for different annealing durations.

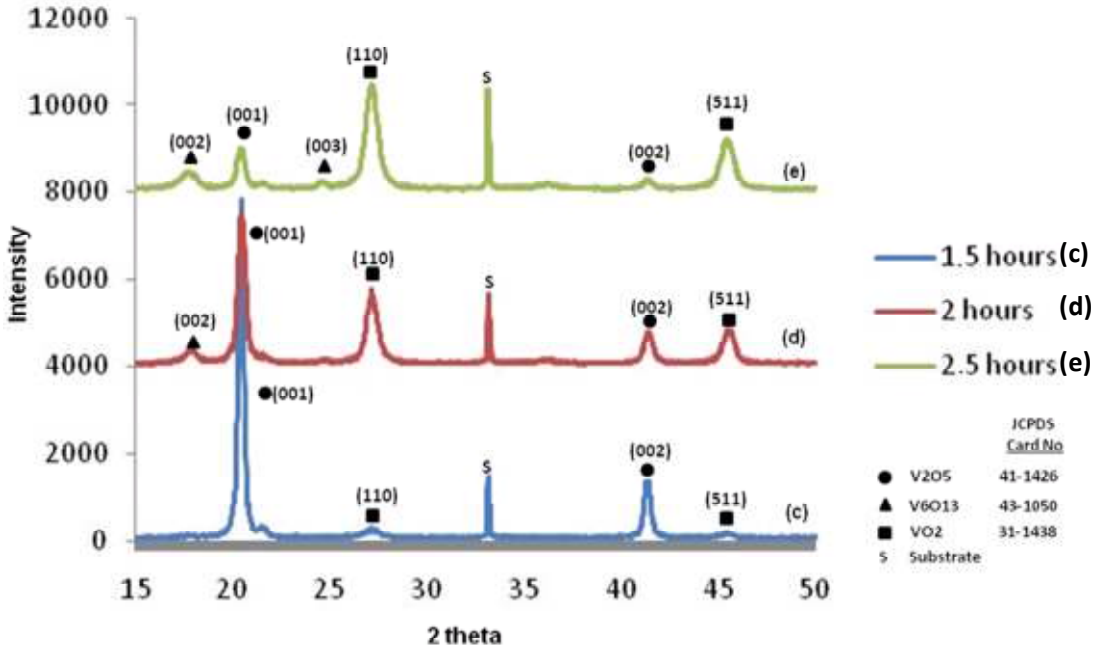

Figure 3.10 – XRD patterns of the films were annealed under 20 % H_2/N_2 environment at 410 °C for (c) 1.5 hours, (d) 2 hours, (e) 2.5 hours and then all films were annealed in N_2 environment at 410 °C for 1 hour.

The major peaks are V_2O_5 (001) and V_2O_5 (002) for the sample (c) which is annealed for 1.5 hours. VO_2 (110) and VO_2 (511) can also be observed however these peaks have very low intensities. There is not any other intermediate VO_x state (V_6O_{13}, V_4O_9) peaks appeared. Sample (c) has mostly orthorhombic V_2O_5 structure.

Sample (d) was annealed for 2 hours under reducing atmosphere. The four major peaks are V_2O_5 (001), V_2O_5 (002), VO_2 (110), and VO_2 (511). The highest intensity peak is V_2O_5 (001). V_2O_5 (002), VO_2 (110), and VO_2 (511) peaks are very close in respect of intensity. V_6O_{13} (002) and V_6O_{13} (003) peaks were also appeared in this sample. There is not any preferred VO_x orientation for sample (d).

The annealing time under 20 % H_2/N_2 atmosphere was prolonged to 2.5 hours, the orientation of the sample (e) closes to the VO_2 orientation. The V_2O_5 and V_6O_{13} peaks can still be observed, however the major peaks are VO_2 (110) and VO_2 (511). The trend of the annealing time by the orientation of the film shows that longer annealing time turns the orientation from V_2O_5 to VO_2.

Annealing time dependency for 30 % H_2/N_2 environment is given in the Figure 3.11. Sample (f), sample (g), and sample (h) were annealed under 30 % H_2/N_2 environment at 410 °C for 1.5 hours, 2 hours, and 2.5 hours respectively.

Many VO_x peaks are observed from the XRD pattern of the sample (f). The highest intensity peak is V_2O_5 (001). V_2O_5 (002), V_6O_{13} (002), V_6O_{13} (110), V_6O_{13} (003), VO_2 (110), and VO_2 (511) peaks are the other VO_x states for this film. It is possible to say that sample (f) has mixed VO_x structure and the x is close to 2.5 (V_2O_5).

The highest peak is changed when the annealing time is prolonged to 2 hours under 30 % H_2/N_2 atmosphere. The highest peak is VO_2 (110) for sample (g). The intensity of the V_2O_5 (001) peak of sample (g) has one fifth lower intensity than the V_2O_5 (001) peak of sample (f). The other V_2O_5 peak is nearly disappeared. V_6O_{13} (002), V_6O_{13} (110), and VO_2 (511) peaks are the other peaks that can be observed in the XRD pattern of this sample. The orientation of the sample (g) is mixed VO_x.

Sample (h) was kept under the 30 % H_2/N_2 atmosphere for 2.5 hours. The orientation of the film is very close to VO_2. V_2O_5 peaks are very close to disappearance. There are other intermediate VO_x state peaks such as V_6O_{13} (002), V_6O_{13} (110), however as it is mentioned VO_2 is the dominant orientation for this sample.

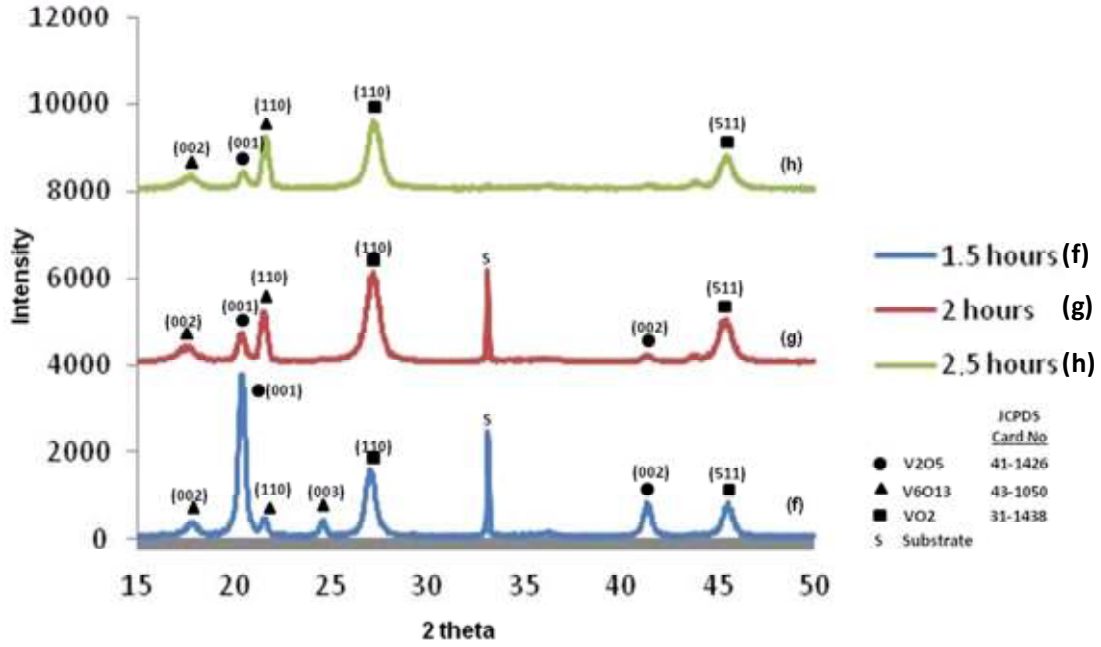

Figure 3.11 – XRD patterns of the films were annealed under 30 % H_2/N_2 environment at 410 °C for (f) 1.5 hours, (g) 2 hours, (h) 2.5 hours and then all films were annealed in N_2 environment at 410 °C for 1 hour.

VO_x structure which is close to VO_2 can be achieved under the 30 % H_2/N_2 atmosphere for 2.5 hours. The effect of higher H_2/N_2 ratio and lower annealing time was tried for two samples. Annealing time dependency of these two samples for 40 % H_2/N_2 environment are given in the Figure 3.12.

1 hour annealed sample (i) has dominant V_2O_5 structure. V_2O_5 (001) and V_2O_5 (002) are the major peaks however, VO_2 peaks are slightly appeared.

Sample (j) was annealed under the 40 % H_2/N_2 atmosphere for 1.5 hours. Mixed VO_x structure is seen from the XRD pattern of this sample. Major peaks are V_2O_5 (001), V_2O_5 (002), V_6O_{13} (110), VO_2 (110), and VO_2 (511). The highest intensity peak is V_2O_5 (001). V_2O_5 (002), V_6O_{13} (110), VO_2 (110), and VO_2 (511) peaks are very close in respect of intensity.

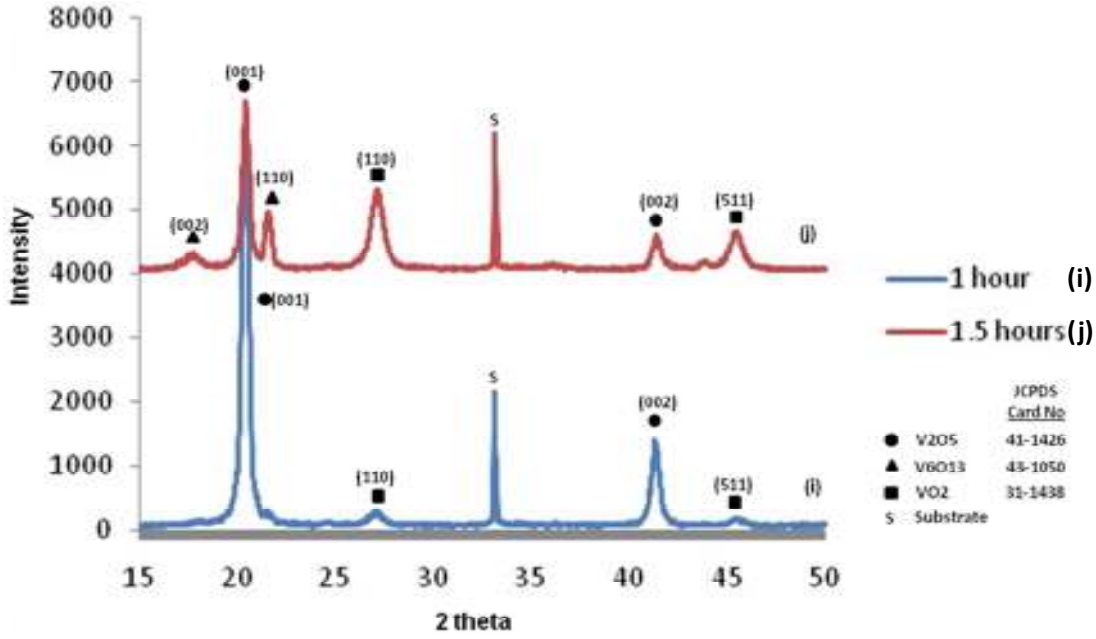

Figure 3.12 – XRD patterns of the films were annealed under 40 % H_2/N_2 environment at 410 °C for (f) 1.5 hours, (g) 2 hours, (h) 2.5 hours and then all films were annealed in N_2 environment at 410 °C for 1 hour.

It is understood from the analysis of the XRD patterns of the films that annealed for different time periods at same environment; the film structure closes from V_2O_5 to VO_2 when the annealing periods prolongs. Intermediate oxygen states of VO_x are also observed between the V_2O_5 and VO_2.

3.3.2. H_2 Concentration Dependency

The same XRD patterns of the samples are presented in respect to the hydrogen concentration of the annealing environment. XRD patterns of the samples which were annealed for same period of time but in different H_2/N_2 ratios environments are evaluated to see the effect of the reducing gas mixture.

Figure 3.13 shows the XRD patterns of three samples which were annealed for 1.5 hours in different H_2/N_2 concentration environments.

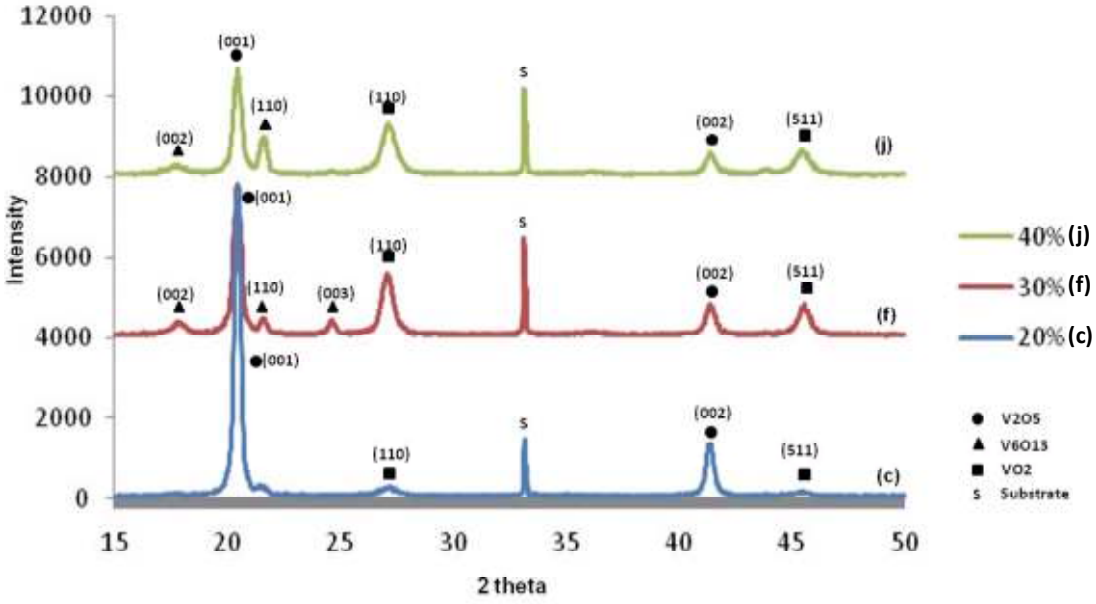

Figure 3.13 – XRD patterns of the films were annealed for 1.5 hours at 410 °C in (c) 20 %, (f) 30 %, (j) 40 % hydrogen concentration of annealing environment and then all films were annealed in N_2 environment at 410 °C for 1 hour.

The hydrogen concentration dependency clearly observed from the results. The major structure is V_2O_5 for the sample (c) which was annealed under 20 % hydrogen concentration. Only very small intensity peaks of VO_2 can be observed. However the orientation of the sample (f) is completely mixed. VO_2 (110) and VO_2 (511) peaks are very clear and V_6O_{13} peaks are also appeared. Furthermore the intensities of the V_2O_5 peaks are at very low when they are compared with the peaks of sample (c). The XRD pattern of sample (j) which was annealed under 30 % concentration is very close to pattern of the sample (f). Any hydrogen concentration dependent difference cannot be observed for those two samples.

Figure 3.14 shows the XRD patterns of three samples which were annealed for 2 hours.

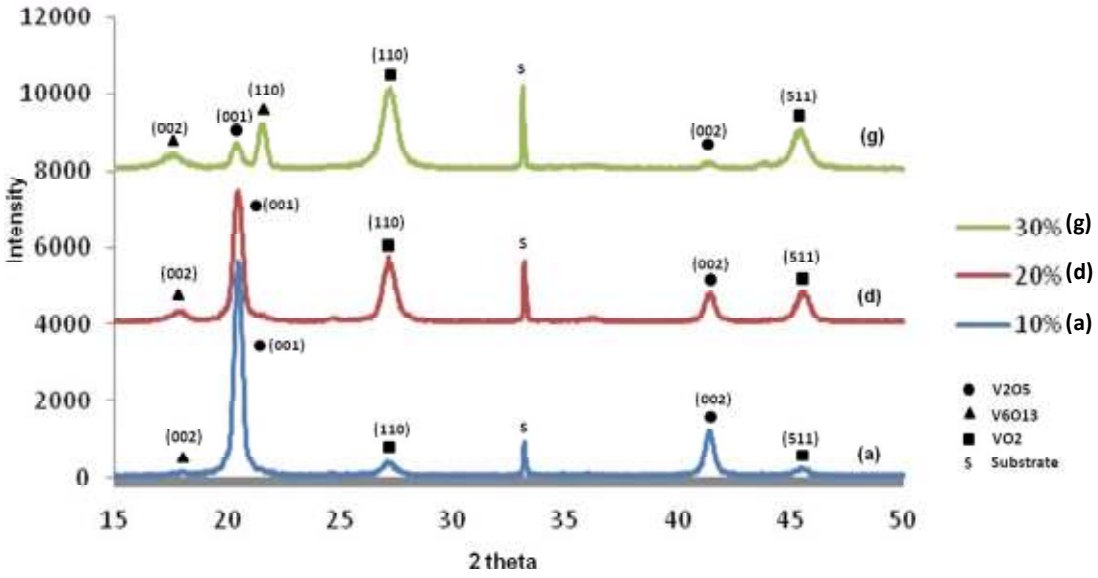

Figure 3.14 – XRD patterns of the films were annealed for 2 hours at 410 °C in (a) 10 %, (d) 20 %, and (g) 30 % hydrogen concentration of annealing environment and then all films were annealed in N_2 environment at 410 °C for 1 hour.

The major structure of sample (a) which was annealed under 10 % hydrogen concentration is V_2O_5 same as the sample (c). Sample (d) has a mixture structure. V_2O_5 (001). V_2O_5 (002), V_6O_{13} (002), VO_2 (110), and VO_2 (511) peaks are observed. The major structure is changed for the sample (g). VO_2 (110) is the major peak and the V_2O_5 peaks has very low intensities for this sample. Remarkable intermediate state V_6O_{13} peaks are also observed in the structure of the film. The hydrogen dependency clearly observed for these samples which were annealed for 2 hours.

Figure 3.15 shows the XRD patterns of three samples which were annealed for 2.5 hours in different H_2/N_2 concentration environments.

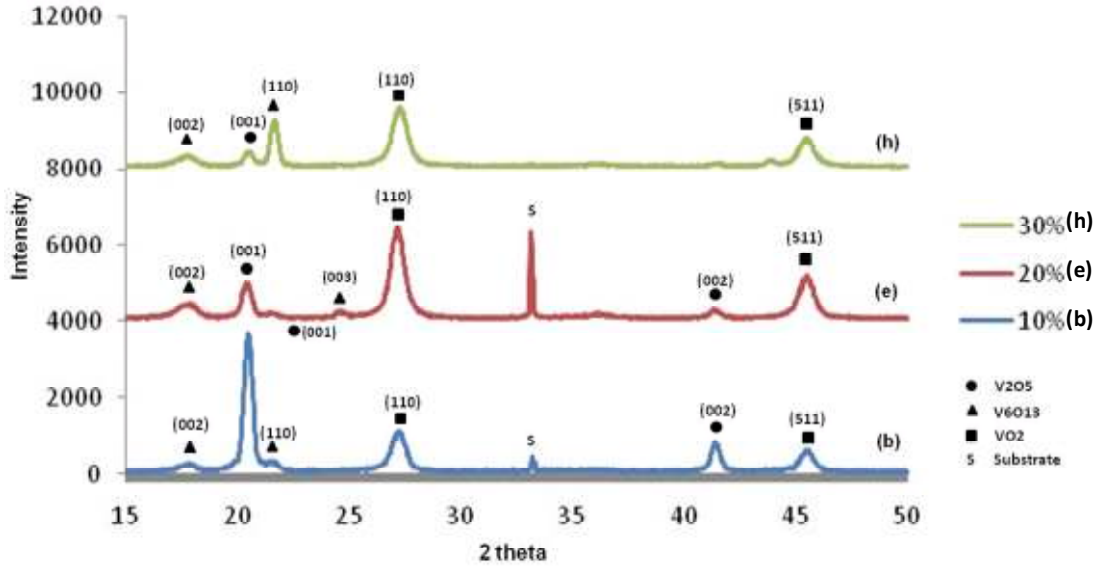

Figure 3.15 – XRD patterns of the films were annealed for 2.5 hours at 410 °C in (a) 10 %, (d) 20 %, and (g) 30 % hydrogen concentration of annealing environment and then all films were annealed in N_2 environment at 410 °C for 1 hour.

There is a major V_2O_5 (001) peak in the XRD pattern of the sample (b) which was annealed under 10 % hydrogen concentration. However the other states are also observed for this sample. It is possible to say that sample (b) has a VO_x structure which is close to V_2O_5. The sample annealed under 20 % hydrogen concentration has a major VO_2 (110) peak. There are also other intermediate state and V_2O_5 peaks in structure of the sample (e). V_2O_5 peaks are completely disappeared for the sample annealed under 30 % hydrogen concentration. VO_2 is the dominant state for this sample. However the intensities are getting to lower values for this annealing condition.

The hydrogen concentration dependency can easily be understood from the above figures. The VO_x structure closes to the VO_2 when the samples were annealed under higher hydrogen concentrations. However, there is a limit for the hydrogen concentration level. Even if the concentration level of hydrogen increased the VO_x structure that is obtained does not change for the small period of time annealing. For

longer period annealing the concentration of the hydrogen should be determined at appropriate value.

3.3.3. Reproducibility (Annealing)

The reproducibility of the annealing process is an important factor for the complete set of the experiment. To see the annealing repeatability, three samples were annealed under same conditions and their XRD patterns are presented in Figure 3.16. The XRD patterns of three samples are very close to each other.

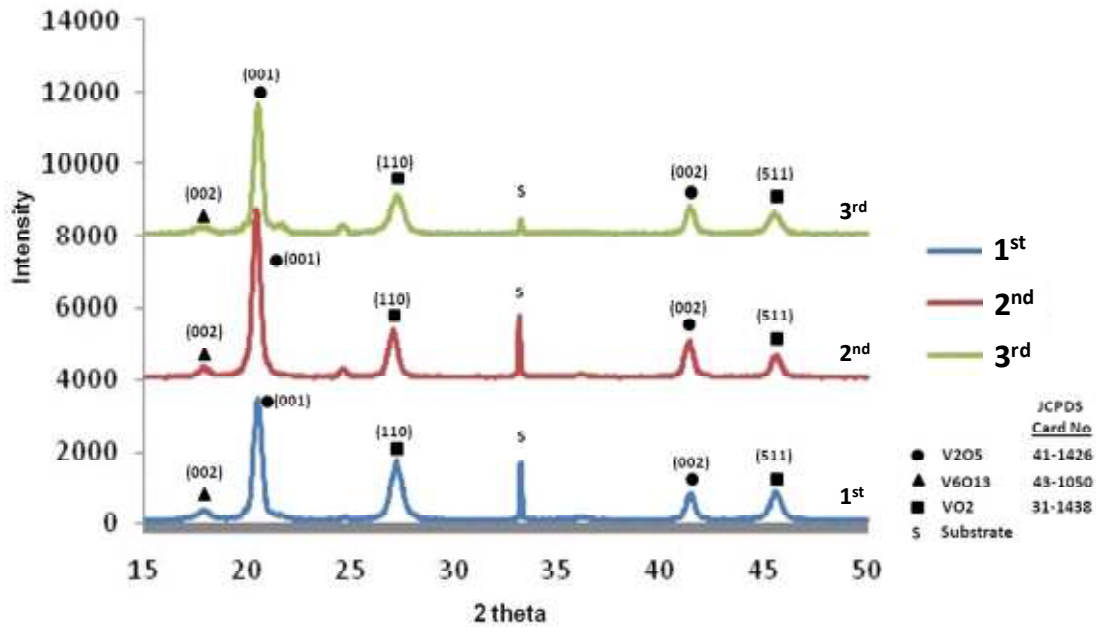

Figure 3.16 – Three samples were annealed under 20 % hydrogen concentration for 2 hours at 410 °C.

It is understood from the XRD patterns of the samples that it is not possible to achieve single crystal VO_2 structured thin films annealing the sol gel deposited V_2O_5 thin films under H_2/N_2 environment. The film structure becomes amorphous with prolonged annealing duration or higher hydrogen concentration of annealing environment.

CHAPTER 4

PERFORMANCE OF SOL-GEL DEPOSITED VO_x THIN FILMS

This chapter presents the performance of the sol-gel growth VO_x thin films. Section 4.1 defines the methods and procedures of sheet resistance, Temperature Coefficient of Resistance (TCR), and noise measurements. Section 4.2 gives the results of the measurements.

4.1. Measurement Methods

4.1.1. Sheet Resistance Measurement Method

The sheet resistance values of the thin films give an opinion about the relation between the VO_x structure and the sheet resistance. The sheet resistances of the thin films were measured with four point probe technique. In this study Signatone QaudPro Automatic System was used for four point probe measurements. Figure 4.1 shows the four point probe measurement system.

Basic working principle of a four-point probe is measuring sheet resistance of a thin film on an insulating substrate. If the surface does not an insulator the sheet resistance cannot be measured. In this study, sheet resistances of thin films that were coated on SiN_x substrates were measured by four point probe.

There are two probes which are connected a current supply are placed outer side of all dour point probes. The other two probes measure the voltage between two probes. When the current applied, the voltage change is read from the inner probes. Figure 4.2 and Figure 4.3 show the probe structure of the measurement system. The

relationship between current and voltage is dependent to the resistivity feature of the thin film.

Figure 4.1 – QuadPro Four point probe measurement tool was used to measure the sheet resistances of VO_x thin films.

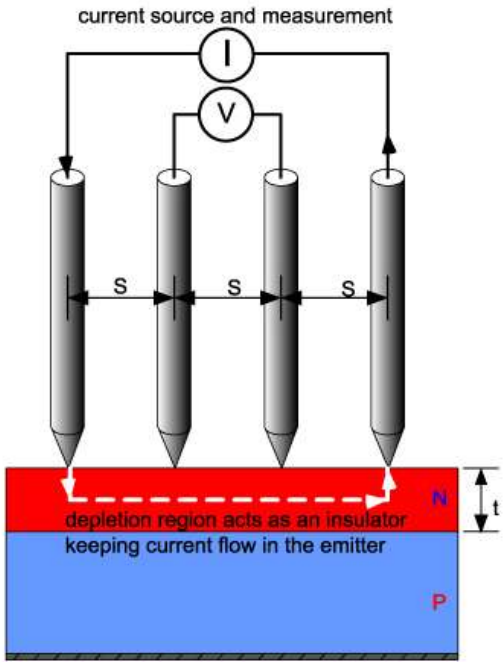

Figure 4.2 – Four point probe measurement of semiconductor sheet resistance [53].

$$R_{sheet} = \rho V / I \tag{4.1}$$

where R_{sheet} is the sheet resistance, V is the voltage between the inner probes and I is the applied current between the outer probes. ρ (rho) is the geometric correction factor for thin film measured on four-point probe, which equals to π/ln2.

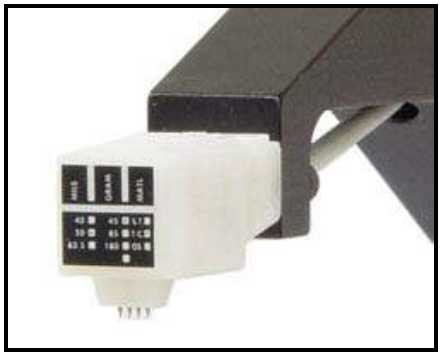

Figure 4.3 – QuadPro four point probe head.

4.1.2. TCR and Noise Measurements

After the sheet resistance measurements and understanding the relation between the VO_x thin films and sheet resistance, two electrode wafers were spin coated and annealed in chosen environments which had better sheet resistance values.

Fabrication of the electrode wafers which were used in this study is as follows:

0.2 μm silicon nitride is deposited on top of the 4 inch silicon wafer as an isolation layer. 20 nm titanium layer is coated on top of the nitride layer. 75 nm gold layer is coated on top of the Ti layer. PR S1813 (photoresist) is coated on top of the metal layer. This layer exposed and the PR is developed. 20 minutes hard bake was done after development. After hard bake, by using gold and titanium wet etches respectively, etchings of the metal layers were done. PR is removed by holding the

wafer in acetone for 20 minutes. Figure 4.4 shows the planar resistors on the electrode wafer. Some of the planar resistors have finger structures.

(a) (b)

Figure 4.4 – Electrode wafer (a) finger planar resist, (b) normal planar resist.

Electrode wafers were spin coated with two step processing. As it was applied on the other successful coatings, first step was at lower spinning rate for 5 seconds and the second step was at 2000 rpm for 75 seconds. The wafers were coated properly without defects.

(a) (b) (c)

Figure 4.5 – (a) Spin coater (METU-MEMS clean room) (b) the wafer was put on to the chuck of the spin coater (c) the solution was put on the electrode wafer.

They were annealed at same temperatures however at different atmospheres and for different periods. One of the samples was annealed in 20 % H_2N_2 environment at

410 °C for 2.5 hours. The other sample was annealed in 30 % H_2N_2 environment at 410 °C for 2 hours. Figure 4.6 shows the both samples which were annealed in N_2 environment at 410 °C for 1 hour after the reduction annealing.

(a) (b) (c)

Figure 4.6 – (a) right after the VO_x solution coated on the electrode wafer (b) the wafer was annealed under 20 % H_2N_2 environment at 410 °C for 2.5 hours (c) same wafer annealed under N_2 environment at 410 °C for 1 hour.

Coated and annealed wafers were kept in 110 °C oven before the primer and photo resist (PR) coating. Before the PR coating process Primer was coated to remove the OH groups from the surface and let the PR stick to the surface of the wafer. Primer was coated at 4000 rpm. PR 51813 was coated at 4000 rpm. After spin coating of primer and PR, wafers were soft baked at 115 °C on hot plate for one minute and thirty seconds. Lithography was done to the samples on the EV Group EVG 620 lithography and aligner. Figure 4.7 shows the lithography device. The radiation was exposed on to the samples for 4.5 seconds. Samples were put in to developer (MF 319) for three minutes and then they were hard baked at 110 °C for twenty minutes.

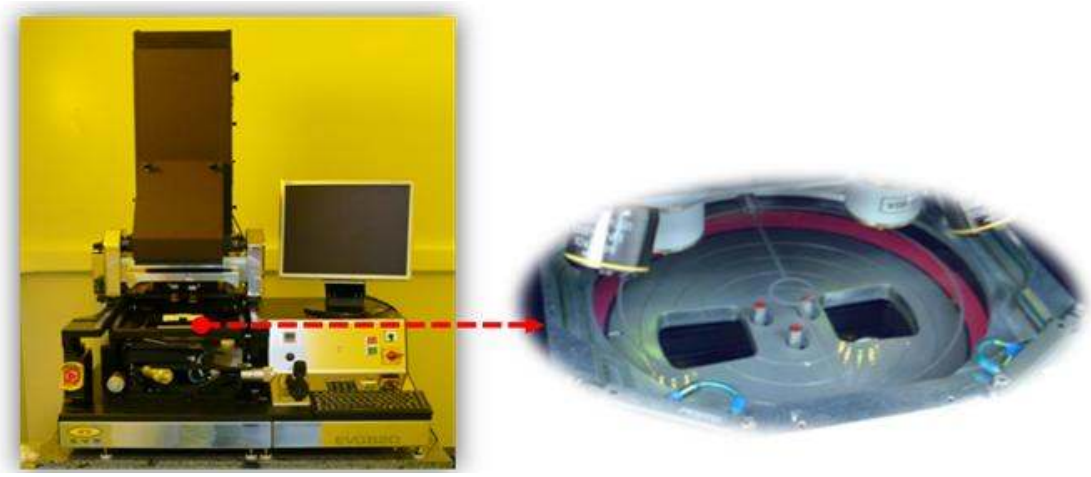

Figure 4.7 – EV Group EVG 620 lithography and aligner located at METU-MEMS clean room.

Lithography basically described as desired pattern is transferred on to the PR coated wafer by exposing radiation. The physical property of a PR, a photo sensitive material, is changed when the radiation exposes on it. Figure 4.8 shows the mask which allows exposing the radiation only the desired area.

Before the wet etching process the wafers were broken to dies to try different etchants. The list of the etchants that were used is given at below:

a) H_2O_2 (30 %) : DI-Water (1 : 20)
b) H_2O_2 (30 %)
c) Hydrochloric acid (36 wt %) : DI-Water (1 : 24)
d) Nitric acid (70 wt %) : DI Water (1 : 1)
e) Sulfuric Acid (98 wt %) : DI Water (1 : 2)

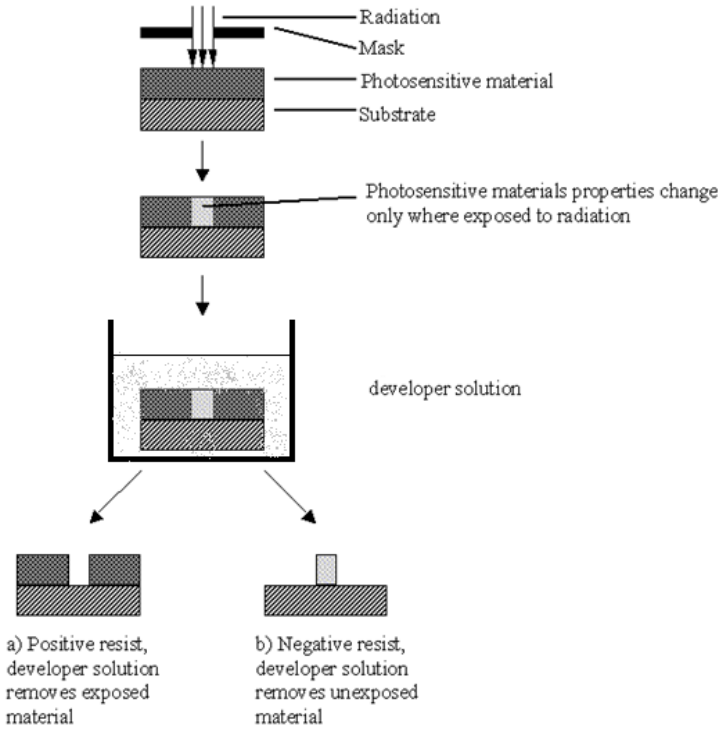

Figure 4.8 – Common steps of a lithography process [54].

The first three etchants were not successful to etch the VO_x at the openings. Nitric acid and sulfuric acid etchants were better than the others. However, nitric acid and sulfuric acid could not completely etch the vanadium, so the remaining vanadium was scratch out from the electrode surfaces by pinpoint. The etched and cleared wafers were wire bonded for resistance, TCR, and noise measurements.

TCR measurements were done between 15 °C to 45 °C. Noise measurements were done in 27 kHz bandwidth.

4.2. Results of The Measurements

4.2.1. Sheet Resistance Results

Sheet resistance is one of the performance parameters of the thin films. The sheet resistances of the films that were successfully coated and annealed were measured by four point probe. The results are presented in Table 4.1.

Table 4.1 – The sheet resistance values and the VO_x structure of the samples. Light grey colored samples are V_2O_5 structured and dark grey colored samples are reduced VO_x structured.

Sample #	Annealing #	Mean Sheet Resistance (M.Ω/sqr)	VO_x
7.1_E	2	27.3	V_2O_5
6.1_C	3	63	V_2O_5
6.1_P	5	58	V_2O_5
6.1_G	7	30	V_2O_5
6.1_E_2	8	No contact	?
6.1_E_1	9	No contact	?
7.1_F	10	22.7	V_2O_5
7.1_G	11	8.04	V_2O_5
7.1_H	12	11.4	V_2O_5
7.1_I	13	28.4	V_2O_5
7.1_J	14	200	V_2O_5
7.1_L	15	52	$V_2O_5 + VO_x$
9-d	16	11.27	$V_2O_5 + VO_x$
9-e	17	3.09	$V_2O_5 + VO_x$
9-f	18	13.6	$V_2O_5 + VO_x$
8-g	19	475	V_2O_5
9-g	20	471	V_2O_5
9-i	21	5.98	VO_x
9-o	22	2.04	VO_x
9-h	23	0.11	$VO_x + VO_2$
9-k	24	3.35	$V_2O_5 + VO_x$
9-l	25	0.2	$VO_x + VO_2$
9-m	26	1.52	$VO_x + VO_2$
9-p	27	7.9	$V_2O_5 + VO_x$
9-n	28	2.74	VO_x

As it is understood from the results, the V_2O_5 structured films have very high sheet resistances compare to the other structured films. The sheet resistances of the V_2O_5

structured films are varied from 10 MΩ/sqr to 400 MΩ/sqr. These values are pretty high to achieve a low noise and low power consuming microbolometer. The sheet resistances of the films that were reduced to lower oxygen states are around 40 to 100 times lower than the sheet resistances of V_2O_5 films. The lowest measured value is 110 kΩ/sqr.

When we evaluate the sheet resistance values of the reduced VO_x samples, the lowest values were measured on the samples which are close to the VO_2 structure.

The sheet resistances of the films are given in the Table 4.2. A correlation between the sheet resistances and the XRD patterns which presented above of the films can be made. The sheet resistances of Sample (e) and sample (g) are the lowest compare to the other samples. Sample (e) was annealed under 20 % hydrogen concentration at 410 °C for 2.5 hours and sample (g) was annealed under 30 % hydrogen concentration at 410 °C for 2 hours. These annealing conditions were chosen for the samples coated on electrode wafers.

Table 4.2 – The sheet resistances of the films. The XRD patterns of these films were presented in previous sections.

H2 Cons.	**10 %**		**20 %**			**30 %**			**40 %**	
Duration	**2h**	**2.5 h**	**1.5 h**	**2 h**	**2.5 h**	**1.5 h**	**2 h**	**2.5 h**	**1 h**	**1.5 h**
Sample	**(a)**	**(b)**	**(c)**	**(d)**	**(e)**	**(f)**	**(g)**	**(h)**	**(i)**	**(j)**
	9_e	**9_f**	**9_g**	**9_i**	**9_h**	**9_k**	**9_l**	**9_m**	**9_p**	**9_n**
1	4.28	16	502	8.0	0.116	2.96	0.212	1.99	21.2	3.98
2	1.49	5.8	490	7.7	0.156	4.20	0.257	0.19	7.74	1.56
3	3.5	16	423	4.2	0.059	2.89	0.134	2.62	0.25	2.68
AVARAGE	3.09	13.60	471.67	5.98	0.110	3.35	0.20	1.52	7.90	2.74

*M.Ω/sqr

4.2.2. TCR and Noise Measurement Results

As it is mentioned above, the films that are coated on the electrode wafers were annealed under the same annealing conditions of sample (e) and sample (g). At the end of the preparation process, the wet etching of vanadium was not so successful. Some of the vanadium was etched, however it is not removed completely from top of the electrodes. The remaining vanadium was scratched from the surface by a pinhead. The noise values of the samples directly affected from this not etched and scratched electrodes.

Sample – 1 and Sample – 2 were coated on the electrode wafers. Sample-1 was annealed under 20 % hydrogen concentration at 410 °C for 2.5 hours. Sample-2 was annealed under 20 % hydrogen concentration at 410 °C for 2 hours. Both samples were annealed under N_2 atmosphere at 410 °C for 1hour. After all the production steps of Sample-1 and Sample-2, they were wire bonded for the performance measurements.

The resistance of Sample – 1 was measured around 18 kΩ. For TCR measurement 20 μA bias was applied and the voltage was measured. The resistance of the Sample – 1 was calculated from the applied bias and the measured voltage values. Figure 4.9 shows the resistance change of the Sample – 1 due to the temperature change under 20 μA bias.

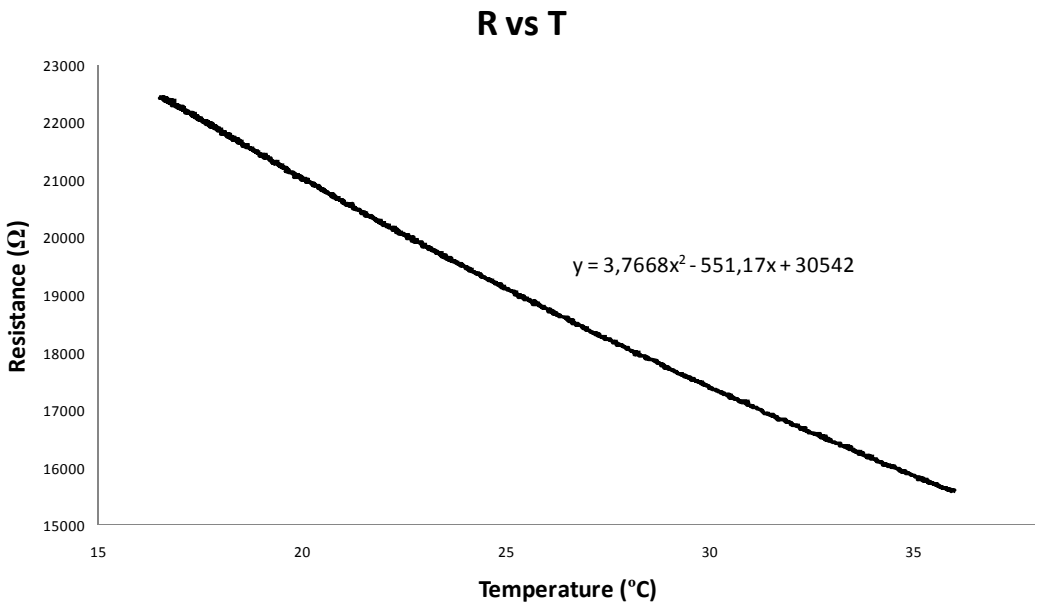

Figure 4.9 – Resistance vs Temperature trend of Sample – 1.

TCR of the Sample – 1 is measured around -1.9 %/ºC at room temperature (25 °C). TCR values for every temperature step are calculated by the following equations.

$$\alpha = \frac{1}{R}\frac{dR}{dT} \tag{4.2}$$

$$TCR = 100x\frac{1}{R(T)}\frac{dR(T)}{dT} \tag{4.3}$$

$$\frac{dR}{dT} = 2 \times 3.76 \times T - (-551.17) \tag{4.4}$$

Resistance chance of Sample-1 due to the temperature change is calculated from R vs T curve of the sample and written as equation (4.4). Figure 4.10 shows the TCR curve of the Sample – 1.

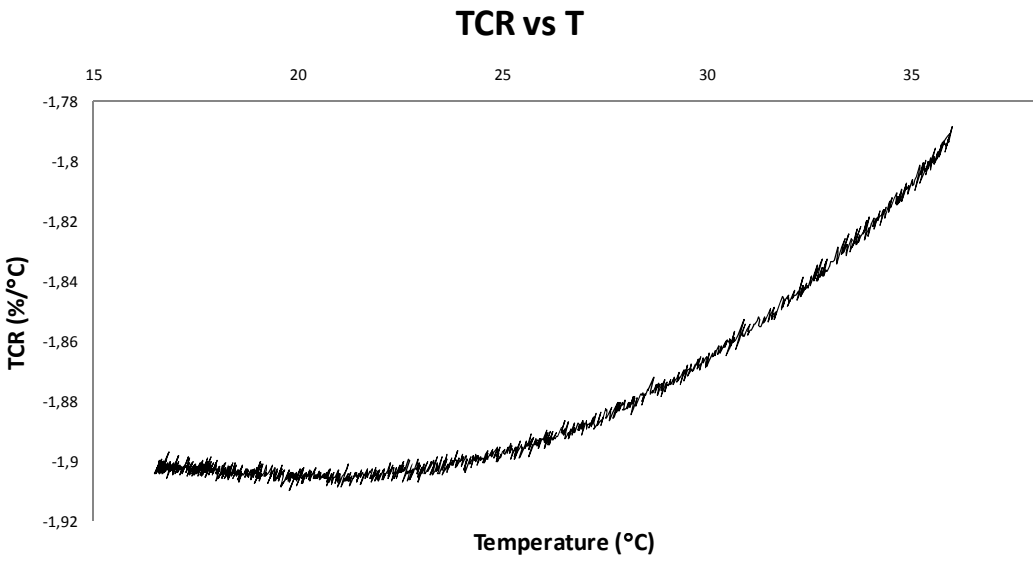

Figure 4.10 – TCR trend of Sample – 1.

The resistance of Sample – 2 was measured around 130 kΩ. TCR measurement was done under 20 μA bias. Figure 4.11 shows the resistance change of the Sample – 2 due to the temperature change under 20 μA bias.

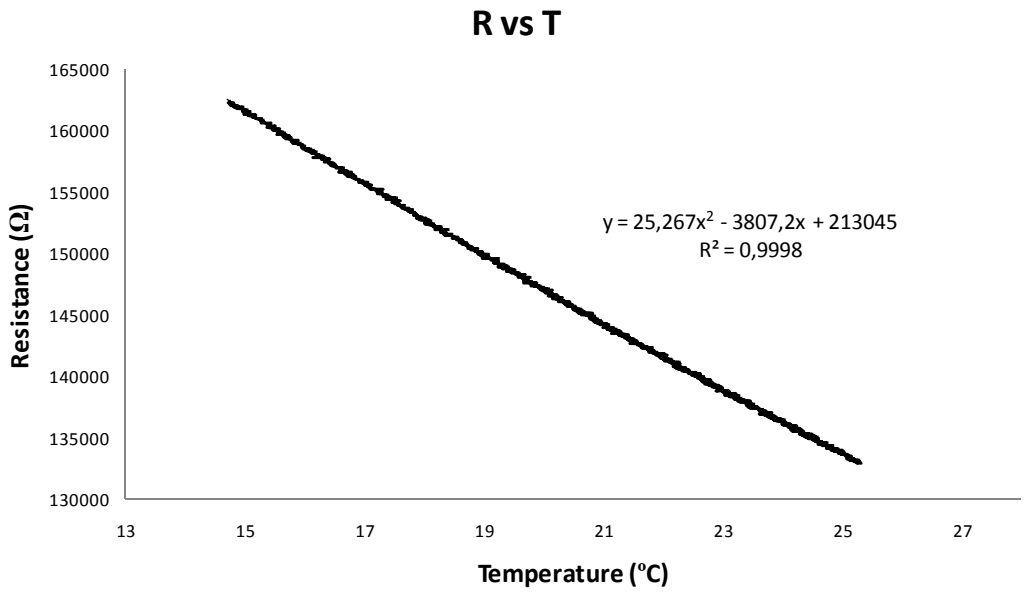

Figure 4.11 – Resistance vs Temperature trend of Sample – 2.

TCR of the Sample – 2 is measured around -1.87 %/ºC at room temperature (25 ºC). TCR values for every temperature step are calculated by the following equations.

$$\frac{dR}{dT} = 2 \times 25.27 \times T - (-3807.2) \tag{4.5}$$

Resistance chance of Sample – 2 due to the temperature change is calculated from R vs T curve of the sample and written as equation (4.5). Figure 4.12 shows the TCR curve of the Sample – 2.

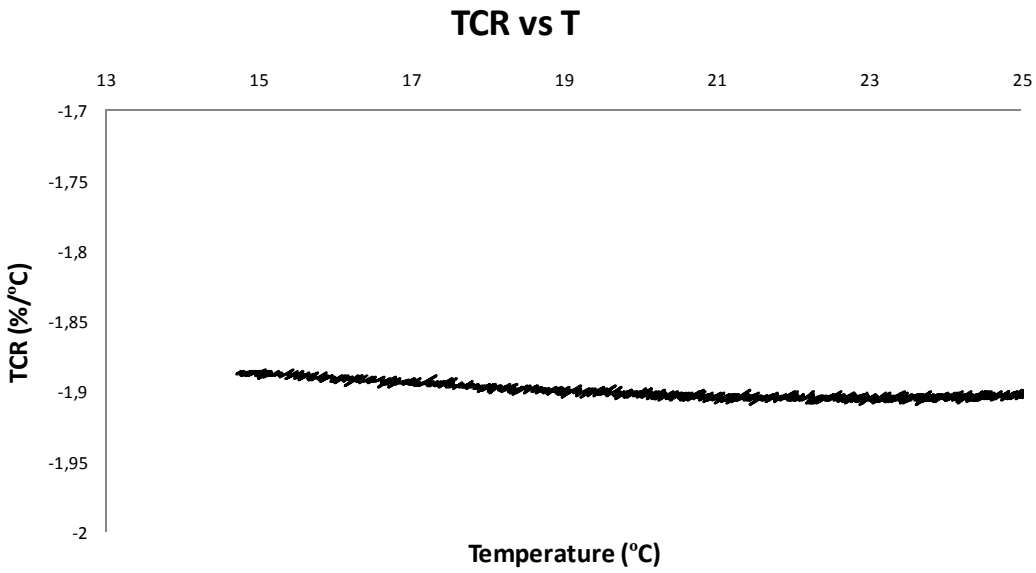

Figure 4.12 – TCR trend of Sample – 2.

The noise measurement of Sample – 1 was done under 20 μA bias. The resistance of the Sample – 1 measured 50 kΩ. Different resistance structure of same electrode wafer was used to make the noise measurement. Figure 4.13 shows the noise power spectral density of Sample – 1.

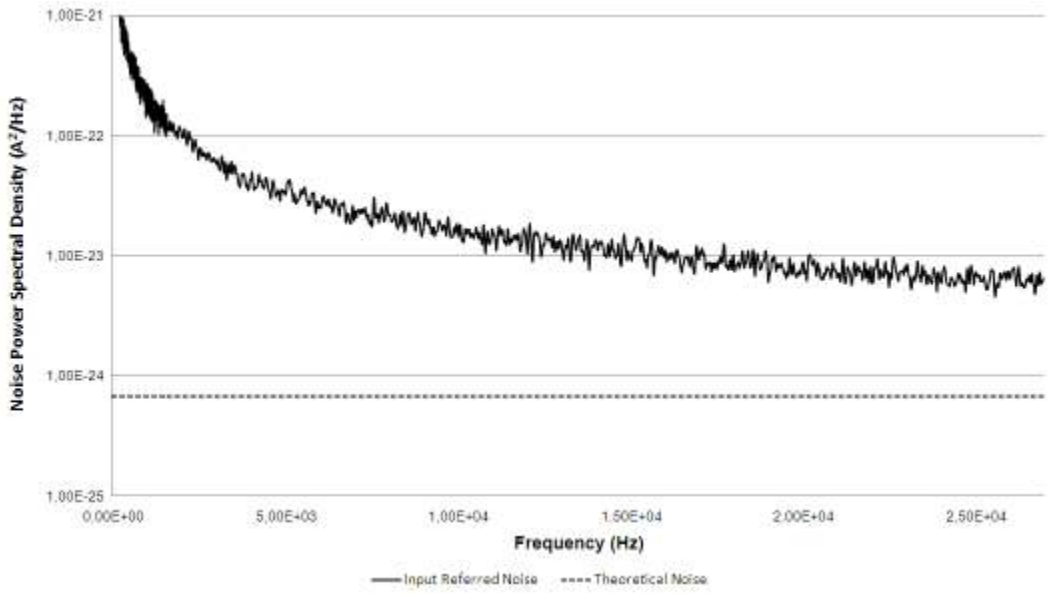

Figure 4.13 – Noise Power Spectral Density vs Frequency of Sample – 1, 50 kΩ resistance under 20 μA bias.

Table 4.3 shows the RMS noise values of Sample-1 in respect to bandwidth.

Table 4.3 – RMS Noise Values of Sample – 1.

RMS Noise Values	
0.5 V	
@4.2 kHz	1.28×10^{-09}
@4.6 kHz	1.29×10^{-09}
@8.4 kHz	1.32×10^{-09}
@9.3 kHz	1.33×10^{-09}
@16.8 kHz	1.37×10^{-09}
@18.5 kHz	1.37×10^{-09}
@27 kHz	1.40×10^{-09}

The noise measurement of Sample – 2 was done under 10 μA bias. The noise measurement set up cannot measure the noise of the sample if the resistance of the sample is high. To make the noise measurement of Sample – 2 the bias current was

decreased from 20 µA to 10 µA. The resistance of the Sample – 2 measured 250 kΩ. Figure 4.14 shows the noise power spectral density of Sample – 2.

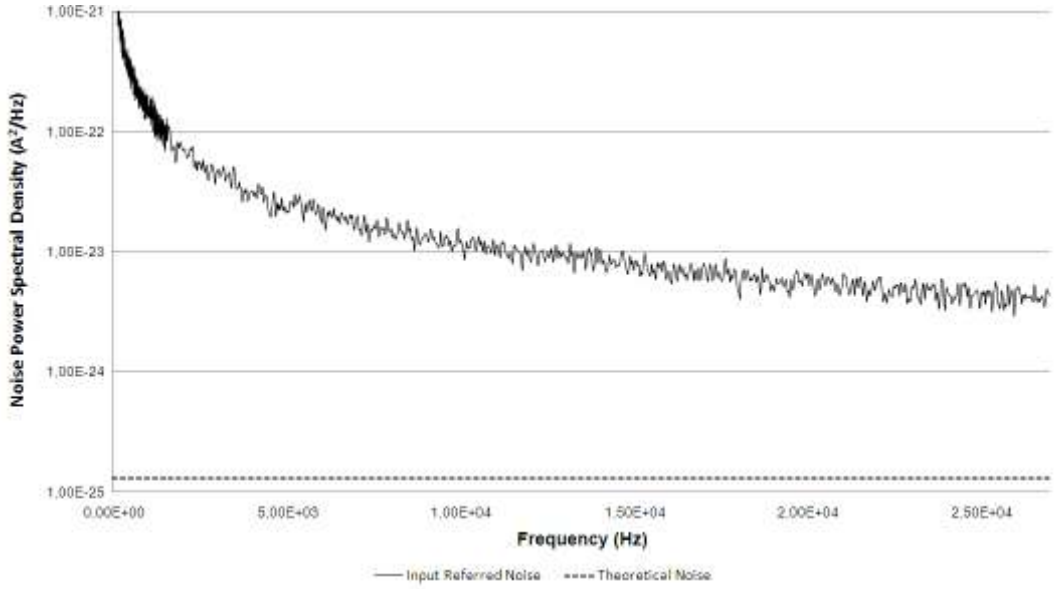

Figure 4.14 – Noise Power Spectral Density vs Frequency of Sample-1, 250 kΩ resistance under 10 µA bias.

Table 4.4 shows the RMS noise values of Sample – 2 in respect to bandwidth.

Table 4.4 – RMS Noise Values of Sample – 2.

RMS Noise Values	
0.5 V	
@4.2 kHz	1.10×10^{-09}
@4.6 kHz	1.10×10^{-09}
@8.4 kHz	1.14×10^{-09}
@9.3 kHz	1.14×10^{-09}
@16.8 kHz	1.17×10^{-09}
@18.5 kHz	1.18×10^{-09}
@27 kHz	1.20×10^{-09}

The noise values of the samples are higher than the expected values which are around a hundred pico-amperes. Possibly the insufficient etching of vanadium from on top of the electrodes causes this unexpected raise of noise values. If the etching is done with an appropriate etchant, the noise values will close to the thermal noise limits.

The corner frequencies of the samples are calculated and presented below.

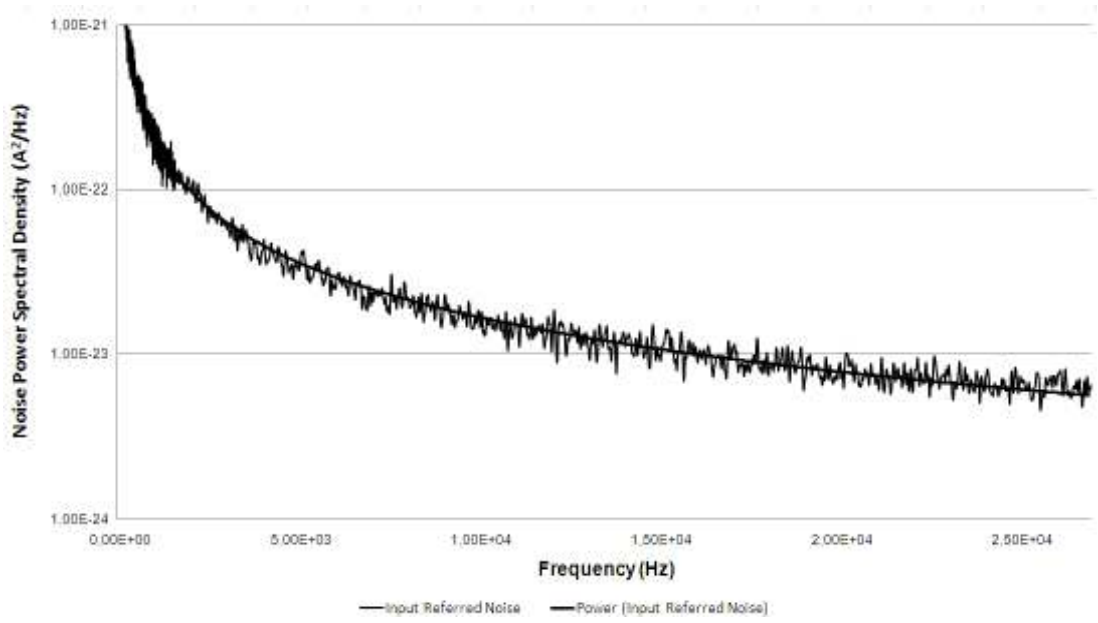

Figure 4.15 – Noise Power Spectral Density and Frequency slope of Sample – 1.

The equation of the slope (Sample – 1) can be written as

$$3.9x10^{-19}\frac{1}{f^{1.09}} + 7.0x10^{-25} \tag{4.6}$$

$7.0x10^{-25}$ is thermal noise and f is the corner frequency. Corner frequency can be calculated from this equation.

$$7.0x10^{-25} = 3.9x10^{-19}\frac{1}{f^{1.09}} \tag{4.7}$$

$$f_c = \left(\frac{3.9x10^{-19}}{7.0x10^{-25}}\right)^{1/1.09} \Rightarrow f_c = 187kHz \tag{4.8}$$

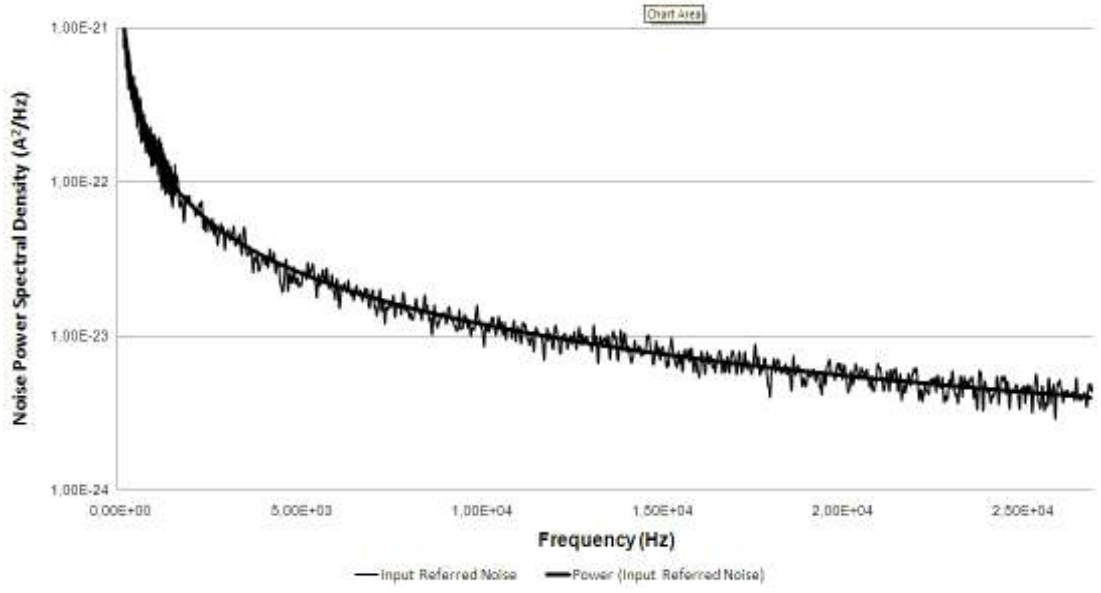

Figure 4.16 – Noise Power Spectral Density and Frequency slope of Sample – 2.

The equation of the slope (Sample – 2) can be written as

$$4.07x10^{-19}\frac{1}{f^{1.3}} + 1.31x10^{-25} \tag{4.9}$$

$1.31x10^{-25}$ is thermal noise and f is the corner frequency. Corner frequency can be calculated from this equation.

$$1.31x10^{-25} = 4.07x10^{-19}\frac{1}{f^{1.3}} \tag{4.10}$$

$$f_c = \left(\frac{4.07x10^{-19}}{1.31x10^{-25}} \right)^{1/1.3} \Rightarrow f_c = 4.04MHz \tag{4.11}$$

The performance critique characteristics of the thin films were measured. The sheet resistance, resistance, and TCR values of the thin films were promising for using the films in a microbolometer application. However, the noise values are pretty high, but they can be improved by using appropriate etchant to remove the VOx from on top of the electrodes. The following chapter presents the conclusions of the whole study, and discusses the future work to improve the results.

CHAPTER 5

CONCLUSIONS

This chapter presents the main results obtained from this study. Sol-gel VO_x coating solutions were formed by mixing DI water and solid vanadium material which is a solid product of dissolution of hydrogen proxide and vanadium metal powder. The solution was spin coated on Si and SiN_x wafers. Process conditions and especially annealing step play the key roles in maintaining the desired film quality. Annealing environment and annealing period were the main variables of this study. Reducing annealing was done with hydrogen and the concentration of the hydrogen was changed between 10 % and 40 %. The annealing period was varied between 1 hour and 2.5 hours in the reducing atmosphere. Specific findings related to film formation, performance parameters will be summarized as follows:

- Solution preparation and coating parameters: Appropriate formulation of the solution is a must for uniform, homogeneous and defect free coatings. The mixing ratio of 1 g : 100 ml vanadium powder and hydrogen peroxide has been found to be the most suitable for the purpose of preparing solid vanadium material. The mixing ratio of solid material and DI water have been determined as 1 g : 33 ml respectively. The viscosities of the solutions prepared with described ratios are 5.77±3. The spinning process has two stages which are slower one and the faster one. Spinning rates of the best coating are 500 rpm for 5 seconds and 2000 rpm for 75 seconds. The average thicknesses for the thin films that coated with mentioned spinning process are about 30±3 nm. The films homogenously covered on the surface of Si and SiN_x substrates.

- Effect of annealing environment and annealing duration: The annealing of successfully coated wafers was done in two steps. The first step was done at 410 °C under hydrogen environment providing a reducing atmosphere. Different hydrogen concentrations of reducing annealing were done. XRD results have revealed that the higher hydrogen concentration provide more reducing VO_x molecules. Similarly, if the annealing duration prolonged, the reduced molecule amount is increased. However there is a limit both for concentration of hydrogen and annealing period. Even if the hydrogen concentration increases, the reduction does not start before 1 hour annealing. If the annealing time prolonged more than a value, the crystal structure of the film starts to disappear. The second step of the annealing was done under nitrogen environment at 410 °C for 2 hours. The conditions of the second annealing step were fixed for all trials.

The best reductions were achieved with two different annealing conditions. The first one is under 20 % H_2/N_2 environment at 410 °C for 2.5 hours. The other one is under 30 % H_2/N_2 environment at 410 °C for 2 hours. When the XRD patterns of the films that annealed with these two annealing conditions they show similarities. The highest peak is VO_2 (110). The intensity of the V_2O_5 (001) peak which is the highest peak before reduction is lowered. The other V_2O_5 peaks are nearly disappeared. V_6O_{13} (002), V_6O_{13} (110), and VO_2 (511) peaks are the other peaks that can be observed in the XRD pattern of these samples. The orientation of these samples is mixed VO_x. The samples annealed by these conditions give the lowest sheet resistance values. Their sheet resistances are in the range of 100 kΩ/sqr – 200 kΩ/sqr.

Two electrode wafers were coated and annealed under the conditions that are described above. Resistance, TCR, and noise measurements were done to see the performance of the thin films. The resistances are 18 kΩ and 130 kΩ under 20 μA bias. The TCR values of the samples measured around -1.9 %/°C at room temperature (25 °C). The noise values were a little bit higher than expected. There are many things that directly affect the noise. The etching of vanadium from on top

of the electrodes is inadequate. This may cause the undesired raise in the noise. The corner frequencies are 187 kHz and 4.04 MHz.

From the results it can be concluded that, it is possible obtain mixed VO_x thin film by using appropriate sol preparation processes and annealing conditions. The resistance values of such VO_x structured films are lower than V_2O_5 structured thin films. The TCR values of these films are high enough to use in a microbolometer application. However, the etching process which is used to remove the excess VO_x layer from on top of the electrodes should be developed to achieve lower noise values.

REFERENCES

[1] F. Niklaus, "*MEMS-Based Uncooled Infrared Bolometer Arrays – A Review*," MEMS/MOEMS Technologies and Applications III, edited by J. C. Chiao, X. Chen, Z. Zhou, and Xinxin Li, SPIE, vol. 6836, pp. 1-5, 2007.

[2] R. B. Darling and S. Iwanaga, "Structure, properties, and MEMS and microelectronic applications of vanadium oxides," *Sadhana*, vol. 34, part. 4, pp. 531-542, 2009.

[3] J. Nag and R. F. Haglund, "Synthesis of Vanadium dioxide thin films and nanoparticles," *Journal of Physics Condensed Matter*, vol. 20, pp. 1-14, 2008.

[4] J. Livage and D. Ganguli, "Sol-gel electrochromic coatings and devices: A review," *Solar Energy Materials & Solar Cells*, vol. 68, pp. 365-381, 2001.

[5] A. Daniels, "*Field Guide to Infrared Systems*," SPIE Press, 2007.

[6] http://www.thefullwiki.org/Infrared, last visited on 06.07.2011

[7] P. W. Kruse, "*Principles of Uncooled Infrared Focal Plane Arrays,*" edited by P. W. Kruse and D. D. Skatrud, Academic Press, 1997.

[8] C. Beşikçi, METU EE755 Infrared Devices and Systems Lecture Notes, Fall 2008-2009.

[9] T. Akin, "*CMOS based Thermal Sensors,*" in Advanced Micro and Nanosystems, vol.2, CMOS-MEMS edited by H. Baltes, O. Brand, G. K. Fedder, C. Hierold, J. Korvink, and O. Tabata, Wiley-VHC, 2005.

[10] M. Y. Tanrıkulu, "An Uncooled Infrared Microbolometer Detector Array Using Surface Micromachined MEMS Technology," *Dissertation for The*

Degree of Doctor of Philosophy, Middle East Technical University, Department of Electrical and Electronics Engineering, 2007.

[11] J. J. Yon, L. Biancardini, E. Mottin, J. L. Tissot, and L. Letellier, "Infrared microbolometer sensors and their application in automotive safety," *Advanced Microsystems for Automotive Applications 2003*, pp. 1-15, 2003.

[12] R. A. Wood, "*Monolithic Sislicon Microbolometer Arrays,*" in Uncooled Infrared Imaging Arrays and Systems, edited by P. W. Kruse, and D. D. Skatrud, Academic Press, 1997.

[13] N. T. Gordon and I. M. Baker, "*Assesment of Infrared Materials and Devices,*" in Infrared Detectors and Emmiters: Materials and Devices, edited by P. Capper and C. T. Elliott, Kluwer Academic Publishers, 2001.

[14] Y. Lv, M. Hu, M. Wu, and Z.Liu, "Preparation of vanadium oxide thin films with high temperature coefficient resistance by facing target d.c. reactive sputtering and annealing process," *Surface and Coatings Technology*, vol. 201, pp. 4969-4972, 2007.

[15] P. W. Kruse, "*Uncooled Thermal Imaging,*" SPIE Press, 2001.

[16] R. K. Bhan, R. S. Saxena, C. R. Jalwania, and S. K. Lomash, "Uncooled Infrared Microbolometer Arrays and Their Characterisation Techniques," *Defence Science Journal*, vol. 59, no .6, pp.580-589, 2009.

[17] S. Chiussia, C. Serraa, J. Serraa, P. Gonzáleza, B. Leóna, S. Urbanb, G. Andräb, J. Bergmannb, F. Falkb, F. Fabbric, L. Fornarinic, S. Martellic, F. Rinaldic, "Laser crystallisation of poly-SiGe for microbolometers," *Applied Surface Science,* vol. 186, issues 1–4, pp.166–172, 28 January 2002.

[18] J. Dai, X. Wang, S. He, Y. Huang, X. Yi, "Low temperature fabrication of VO_x thin films for uncooled IR detectors by direct current reactive magnetron

sputtering method," *Infrared Physics and Technology,* vol.51, pp. 287-291, 2008.

[19] Y. Lv, M. Hu, M. Wu, and Z. Liu, "Preparation of vanadium oxide thin films with high temperature coefficient of resistance by facing targets d.c. reactive sputtering and annealing process," *Surface and Coatings Technology*, vol. 201, issues 9-11, pp. 4969-4972, 2007.

[20] K. M. Park, "Optimum O_2 concentration for the optoelectronic properties of IR sensitive VO_x thin films," *Optical Materials*, vol. 17, pp. 311-314, 2001.

[21] W. Lixia, L. Jianping, G. Xiaoguang, and H. Xiuli, "Effects of deposition parameters on the properties of VO_2 thin films," *Progress in Natural Science*, vol. 16, issue 11, pp.1193 – 1197, 2006.

[22] "*Handbook of Sol–Gel Science and Technology Processing, Characterization and Applications*," edited by S. Sakka, Volume I: Sol–Gel Processing, Volume edited by H. Kozuka, Kluwer Academic Publishers, 2004.

[23] C. J. Brinker and G. W. Scherer, "*Sol-gel science: the physics and chemistry of sol-gel processing,*" Academic Press inc., 1990.

[24] C. J. Brinker and G. W. Scherer, "*Sol-Gel Science: The physics and chemistry of sol-gel processing,*" Academic Press Inc, pp. 23-30, 1990.

[25] I. Takahashi, M. Hibino, and T. Kudo, "Thermocromic $V_{1-x}W_xO_2$ Thin Films Prepared by Wet Coating Using Polyvanadate Solutions", *Japannese Journal of Applied Physics*, vol. 35, pp. L438-L440, 1996.

[26] Y. Ningyi, L. Jinhua, H. L. W. Chan, and L. Chenglu, "Comparison of VO_2 thin films prepared by inorganic sol-gel and IBED methods," *Applied Physics A*, vol. 78,pp. 777-780, 2004.

[27] Y. Takahashi, M. Kanamori, H. Hashimoto, Y. Moritani, and Y. Masuda, "Preparation of VO_2 films by organometallic vapour deposition and dip coating," *Journal of Materials Science*, vol. 24, pp. 192-198, 1989.

[28] S. Deki, Y. Aoi, and A. Kajinami, "A Novel wet process for the preparation of vanadium dioxide thin film," *Journal of Material Science*, vol. 32, pp. 4269-4273, 1997.

[29] T. Chen, M. Hu, J. Liang, J. Lu, and L. Tan, "Study on Preparation of Vanadium Oxide Thin Films by The Metal-oxygenation Method," *Proceedings of SPIE, International Symposium on Photoelectronic Detection and Imaging 2009: Material and Device Technology for Sensors,* vol. 7381, pp. 738117-1-7, 2009.

[30] A. C. Pierre, "*Introduction to Sol-gel Processing*", Kluwer Academic Publishers, 1998.

[31] D. P. Partlow, S. R. Gurkovich, K. C. Radford, and L. J. Denes, "Switchable vanadium oxide films by a sol-gel process," *Journal of Applied Physics*, vol. 70, pp.443-452, 1991.

[32] B. Alonso and J. Livage, "Synthesis of Vanadium Oxide Gels from Peroxovanadic Acid Solutions: A 51V NMR Study," *Journal of Solid State Chemistry*, vol. 148, pp.16-19, 1999.

[33] J. Livage, G. Guzman, and F. Beteille, "Optical properties of Sol-Gel Derived Vanadium Oxide Films," *Journal of Sol-Gel Science and Technology*, vol. 8, pp. 857-865, 1997.

[34] I. Takahashi, M. Hibino, T. Kudo, "Thermochromic properties of double doped VO_2 thin films fabricated from polyvanadate solutions," *Proceedings of SPIE, Switchable Materials and Flat Panel Displays*, vol. 3788, pp. 26-33, 1999.

[35] L. Li and Z. Yan, "Synthesis and Characterization of Self-Assembled V_2O_5 Mesostructures Intercalated by Polyaniline," *Journal of Natural Gas Chemistry*, vol. 14, pp. 35-39, 2005.

[36] M. Hibino, M. Ugaji, A. Kishimoto, and T. Kudo, "Preparation and lithium intercalation of a new vanadium oxide with a two dimensional structure," *Solid State Ionics*, vol. 79, pp.239-244, 1995.

[37] T. Kudo, Y. Ikeda, T. Watanabe, M. Hibino, M. Miyayama, H. Abe, and K. Kajita, "Amorphous V_2O_5/carbon composites as electrochemical supercapacitor electrodes", *Solid State Ionics*, vol. 153, pp. 833-841, 2002.

[38] G. Wang, L. Wang, and X. Li, "Synthesis and characterization of poly(o-anisidine)/V_2O_5 and poly(o-anthranilic acid)/V_2O_5 nanocomposites," *Polymer International*, vol. 54, pp. 1082–1087, 2005.

[39] W. Avansi, C. Ribeiro, E. R. Leite, and V. R. Mastelaro, "Vanadium Pentoxide Nanostructures: An Effective Control of Morphology and Crystal Structure in Hydrothermal Conditions," *Crystal Growth & Design*, vol. 9, no. 8, pp.3626–3631, 2009.

[40] J. G. Fontenot, J. W. Wiench, M. Pruski, and G. L. Schrader, "Vanadia Gel Synthesis via Peroxovanadate Precursors. 1. In Situ Laser Raman and ^{51}V NMR Characterization of the Gelation Process", *Journal of Physical Chemistry B*., vol. 104, pp.11622-11631, 2000.

[41] Y. Ningyi, L. Jinhua, and L. Chenlu, "Switching property of sol-gel vanadium oxide thin films," *Proceedings of SPIE, Advanced Photonic Sensors and Applications II,* edited by A. K. Asundi, W. Osten, and V. K. Varadan, vol. 4596, pp.16-20, 2001.

[42] Y. Dachuan, X. Niankan, Z. Jingyu, and Z. Xiulin, "High Quality Vanadium Dioxide Films Prepared By An Inorganic Sol-Gel Method," *Materials Research Bulletin*, vol. 31, no. 3, pp. 335-340, 1996.

[43] Y. Ningyi, L. Jinhua, and L. Chenglu, "Valance reduction process from sol-gel V_2O_5 to VO_2 thin films," *Applied Surface Science*, vol. 191, pp.176-180, 2002

[44] L. Jinhua, Y. Ningyi, and X. Jiansheng, "Annealing behavior of the vanadium oxide films prepared by modified ion beam enhanced deposition," *Infrared Detector Materials and Devices*, *SPIE*, vol. 5564, pp. 140-144, 2004.

[45] C. V. Ramana, S. Utsunomiya, R. C. Ewing, and U. Becker, "Formation of V2O3 nanocrystals by thermal reduction of V_2O_5 thin films," *Solid State Communications*, vol. 137, pp. 645-649, 2006.

[46] X. Wei, Z. Wu, T. Wang, X. Xu, J. Tang, and Y. Jiang, "Influence of Substrate temperature on the morphology and thermal resistance of vanadium oxide thin films," *Proceedings of SPIE, Sixth International Conference on Thin Film Physics and Applications*, vol. 6984, pp. 69842K-1-4, 2008.

[47] M. Ugaji, M. Hibino, and T.Kudo, "Evaluation of a New Type of Vanadium Oxide from Peroxo-polyvanadate as aCathode Material for Rechargeable Lithium Batteries," *Journal of Electrochemical Society*, vol. 142, no. 11, pp. 3664-3668, 1995.

[48] T. J. Hanlon, R. E. Walker, J. A. Coath, and M.A. Richardson, "Comparison between vanadium dioxide coatings on glass produced by sputtering, alkoxide and aqueous sol-gel methods," *Thin Solid Films*, vol. 405, pp. 234-237, 2002.

[49] F. Beteille and J. Livage, "Optical Switching in VO_2 Thin Films," *Journal of Sol-Gel Science and Technology*, vol. 13, pp. 915 – 921, 1998.

[50] M. Pan, H. Zhong, S. Wang, J. Liu, Z. Li, X. Chen, and W. Lu, "Properties of VO_2 thin filmprepared with precursor $VO_{(acac)2}$," *Journal of Crystal Growth,* vol. 265, pp. 121–126, 2004.

[51] S. Lu, L. Hou, and F. Gun, "Structure and Optical Property Changes of Sol-Gel Derived VO_2 Thin Films," *Advanced Materials*, vol. 9, no. 3, pp.244-246, 1997.

[52] S. Lu, L. Hou, and F. Gun, "Surface analysis and phase transition of gel-derived VO_2 thin films," *Thin Solid Films,* vol. 353 pp. 40-44, 1999.

[53] http://pvcdrom.pveducation.org/CHARACT/4pp.HTM, last visited on 04.11.2011

[54] http://www.memsnet.org/mems/beginner/lithography.html, last visited on 12.11.2011